Evaluating the radiative fidelity of WRF-driven PALM (v25.04) in high-resolution using RTM: impact of diverse urban morphology and vegetation on short-wave radiation

Jelena Radović[1], Michal Belda[1], Martin Bureš[2], Kryštof Eben[2], Jan Geletič[1,2], Jakub Jura[3], Pavel Krč[2], Hynek Řezníček[2], and Jaroslav Resler[2]

[1]Department of Atmospheric Physics, Faculty of Mathematics and Physics, Charles University Prague, V Holešovičkách 2, 180 00 Prague 8, Czech Republic
[2]Department of Complex Systems, Institute of Computer Science of the Czech Academy of Sciences, Pod Vodárenskou věží 271/2, 182 00 Prague, Czech Republic
[3]Department of Instrumentation and Control Engineering, Faculty of Mechanical Engineering, Czech Technical University in Prague, Technická 4, 166 07 Praha 6, Czech Republic

Correspondence: Jelena Radović (jelena.radovic@matfyz.cuni.cz)

Abstract. Validating urban short-wave radiation in numerical models is non-trivial, as city measurements are heavily influenced by multiple reflections, absorption, and shading processes driven by the three-dimensional urban morphology and vegetation. At the same time, urban micro-scale models are typically forced by only two types of solar radiation inputs: i) field measurements, often represented by the global radiation, rarely by the combination of short-wave and long-wave radiation; and ii) data given from coarser-resolution models. We conduct a novel high-resolution evaluation study of the PALM model (v25.04), driven by the regional WRF model-derived radiative forcing configured in two distinct parameterisation setups, across a multi-episode ensemble spanning from clear-sky to overcast conditions. We validate and quantify PALM's ability to explicitly resolve the spatiotemporal propagation of short-wave radiation and its interaction with heterogeneous urban landscapes against measurements collected from the stations located in morphologically variant urban settings with different solar access. Results demonstrate that PALM resolves urban- and vegetation-induced short-wave radiative exchange (i.e., canyon trapping, vegetation shading, building reflections, interaction with urban surfaces and dynamic timing) with high fidelity regardless of the urban setting. This performance highlights the model's ability to explicitly capture the 3D micro-scale heterogeneity of the urban canopy, providing a detailed representation of radiative interactions and their dynamic timing. The study reveals the dominant role of biases: despite PALM's explicit physical detail, the errors embedded in meso-scale cloud fields and radiation inputs cannot be fully compensated for by the micro-scale model. This work is a benchmark for the validation of high-resolution urban radiative transfer exchanges and shows that future progress in street-scale micrometeorological simulations hinges on rigorous verification of cloud representation and radiative fields in the meso-scale driving data.

1 Introduction

Proper assessment of urban environments using high-resolution environmental prediction models is a prerequisite for improving the well-being of urban dwellers in densely populated built-up areas (Baklanov et al., 2018). The ever-increasing urbanisation (United Nations, 2024), combined with climate change and continuous urban development, is exacerbating existing environmental hazards, such as increased heat stress, disrupted thermal comfort, air pollution, and water scarcity (Lehnert et al., 2023; Vieira Zezzo et al., 2023). Cities comprise complex urban structures with numerous land-cover components (e.g., urban fabric, transit roads, green spaces, water bodies, sports and leisure facilities). Such a configuration of cities alters and unevenly distributes incoming short-wave radiation from the Sun, thereby affecting radiative exchange processes within the urban boundary layer (Freitas et al., 2015; Oke et al., 2017; Liu et al., 2020; Krč et al., 2021; Geletič et al., 2023; Schoetter et al., 2023). The specific set of interactions with incident solar radiation associated with urban trees primarily involves shading, transpiration, and effects on air temperature, among other factors (Wang and Akbari, 2016; Chen et al., 2021; Geletič et al., 2022; Grylls and van Reeuwijk, 2022).

The aforementioned properties of cities exacerbate an already complex process of modelling urban areas and climate, particularly with respect to radiative processes. As spatial resolution increases, the complexity of radiative processes increases. The necessity of a proper understanding of radiation exchange processes in urban environments has been recognised by the World Meteorological Organization (2024), and the need for their accurate representation in numerical models designed for the urban boundary layer has been highlighted by Krč et al. (2021). Given the complexity of a micro-scale urban environment, it is necessary to consider the interactions of buildings and vegetation with short- and long-wave radiation, as well as reflection, scattering, and thermal emission (Salim et al., 2022). The accurate evaluation of the sky view factor (SVF; Krč et al., 2021) is another important aspect of the radiative transfer model (RTM) since it strongly influences the amount of incoming radiation (Gál and Kántor, 2020). Thus, the SVF influences the surface radiation balance and is a key component in describing urban climatology at scales below 100 m (Dirksen et al., 2019). Since the SVF affects the interaction of short-wave and long-wave radiation from the sky and the surface, its proper estimation by numerical models is necessary (Salim et al., 2022).

Recently, in the practical application of high-fidelity modelling results, there has been increasing demand from urban planners, architects, and municipalities for the estimation of biometeorological indices (Matzarakis et al., 2010; Jänicke et al., 2015; Geletič et al., 2021). However, most of these indices are strongly dependent on radiation, typically expressed as mean radiant temperature (MRT; Krč et al., 2021). According to Wallenberg et al. (2020), MRT is the most significant meteorological variable affecting human energy balance and thermal comfort on clear, sunny days. Outdoor MRT combines the impacts of short-wave and long-wave radiation fluxes in outdoor environments. While long-wave radiation is an important component of the overall radiative balance, especially in indoor or shaded environments, short-wave radiation is often the dominant driver of elevated MRT values outdoors, particularly at high solar altitudes and under clear-sky conditions. Although MRT derivation strictly requires integrating both short-wave and long-wave radiation flux densities, the variability of outdoor MRT during the daytime is heavily influenced by short-wave radiation flux (Lee et al., 2014). Short-wave outdoor MRT includes all components of solar radiation: direct, reflected (from surfaces), and sky-diffused radiation. MRT is further used for the calculation of other

biometeorological indices, such as predicted mean vote (PMV; Fanger, 1967), physiologically equivalent temperature (PET; Höppe, 1999), or universal thermal climate index (UTCI; Jendritzky et al., 2012). Given these facts, it is essential to accurately simulate short-wave radiation in the numerical model (Matzarakis et al., 2010).

The theoretical basis and the level of sophistication achieved in the assessment of urban radiation fields rely on modelling approaches that differ in their physical complexity and in the representation of radiative transfer processes. A common starting point is a relatively simple one-dimensional diagnostic model that calculates radiation fluxes through a single vertical column, focusing primarily on radiative exchange in urban geometries with resolved buildings and trees. The radiation calculation methodology typically estimates quantities such as the SVF and MRT required for further thermal index calculations (Middel et al., 2017; Fröhlich et al., 2019). The next level of complexity in the modelling approaches includes incorporating spatial dimensions and indirect effects of wind velocity on long-wave radiation, as well as the production of the spatiotemporal distribution of radiation fluxes. Examples of micro-scale models that rely on the above-mentioned simple techniques include RayMan (Matzarakis et al., 2007, 2010), its successor, steady-state SkyHelios (Matuschek and Matzarakis, 2011), and the Solar and long-wave Environmental Irradiance Geometry model (SOLWEIG; Lindberg et al., 2008). Numerous studies have evaluated these computationally efficient models and used them for radiation fluxes, MRT calculations, and thermal comfort studies (e.g., Chen et al., 2016; Fröhlich and Matzarakis, 2018; Kántor et al., 2018; Aminipouri et al., 2019; Fröhlich et al., 2019; Gál and Kántor, 2020). A more advanced method for assessing urban environments and microclimates is the use of Computational Fluid Dynamics (CFD) models, which, according to Yang et al. (2023), are widely employed for this purpose. Depending on the modelling framework, CFD models can simulate a variety of spatial and temporal scales, resolving physical processes and the city's topography (e.g., buildings, trees) in great detail (Blocken, 2015, 2018; Toparlar et al., 2017; Kubilay et al., 2020). In the CFD space, several models with strong competence and different approaches to assessing radiation transfer processes have emerged: ENVI-met (Bruse et al., 2023a, b), City-LES (Kusaka et al., 2024), the PALM model system (Maronga et al., 2020), and uDALES (Suter et al., 2022). Within the CFD models, the treatment and methodology for radiative transfer processes differ, and to resolve the highly complex radiative exchanges within urban canopies, these microclimate modelling frameworks implement distinct methodologies: (i) the radiosity method, which is a common methodology used to resolve short-wave and long-wave radiative fluxes within the urban canopy layer (Aoyagi and Takahashi, 2012). Physically, this method treats urban facets as diffuse reflectors, allowing the model to explicitly account for multiple reflections of short-wave and long-wave radiation between vertical walls, ground pavements, and tree canopies, while resolving localised building shadows. This technique is utilised within the first version of the PALM's RTM module (Resler et al., 2017; Maronga et al., 2020) and in City-LES (Kusaka et al., 2024). Validation of short-wave and global radiation fluxes using similar methods has been documented in standard microclimate tools such as ENVI-met (Jänicke et al., 2015; Liu et al., 2018; Piselli et al., 2018; Bruse et al., 2023a, b); (ii) the view factor method is another approach which computes the view factors between planar surfaces arbitrarily located to compute radiative exchange (e.g., based on the method in Rao and Sastri (1996)). This method is implemented, e.g., in the UDALES micro-scale model; (iii) more complex radiation schemes for short-wave radiation like the one proposed in Kondo (1994) or Dudhia (1989), and for long-wave radiation scheme as presented in Kondo (1994) or radiative transfer for inhomogeneous atmospheres (RRTM; Mlawer et al., 1997).

The PALM model system offers a variety of techniques for radiation process modelling. The radiation can be prescribed as constant in the configuration, or a realistic diurnal cycle can be modelled by the internal clear-sky model or by the coupled rapid radiative transfer model (RRTM; Hogan and Bozzo, 2018). It is also possible to use values from an external model or measurements supplied in the dynamic driver (initial and boundary condition provider). Interactions of the radiation with the surface (ground, buildings) and plant canopy are modelled by the integrated RTM (Krč et al., 2021). Alternatively, the externally coupled TenStream model (Jakub and Mayer, 2016) can be used. Starting with the simple one-dimensional radiation model, which takes into account only vertical radiation exchange (Maronga et al., 2015), then moving to more complicated options such as the clear-sky model (Maronga et al., 2020), RRTM for general circulation models (RRTMG; Clough et al., 2005) and RTM (Resler et al., 2017; Krč et al., 2021). The last published version of RTM (3.0) (Krč et al., 2021), based on RTM version 1.0 (Resler et al., 2017), explicitly resolves radiative processes in three-dimensional, complex urban environments at street-scale resolutions of meters. Beyond RTM's capability for high-fidelity, what distinguishes PALM from other established microscale models is the methodological coherence it maintains between radiation physics and the initial and boundary conditions governing boundary-layer dynamics. Namely, reproducing the spatio-temporal variability of urban boundary-layer conditions -particularly radiative conditions and associated quantities- with microscale models like City-LES and uDALES, is limited by their atmospheric dynamics initialisation procedures. These modelling frameworks are not designed to work with arbitrarily chosen, temporally evolving, three-dimensional meteorological fields downscaled from meso-scale models; instead, they rely on observational forcing, commonly supplied through measured vertical profiles. On the other hand, this imperative of achieving physical consistency and bridging the atmospheric meso-micro scale-gap is satisfied by PALM's meso-scale nesting (MESO; Kadasch et al., 2021) model,

Previous studies, such as Resler et al. (2017, 2021) and Krč et al. (2021), validated the RTM against observations, while Salim et al. (2022) explored the significance of radiative transfer processes by systematically isolating them in the PALM model. It is worth noting that the direct evaluation of the radiation model using field measurements has not yet been conducted. The studies mentioned above indirectly assess radiation processes by examining surface temperatures, which strongly depend on accurate radiation. Hence, the primary objective of this study is the validation of PALM's ability to simulate short-wave radiation and the investigation of how it modifies both direct and reflected short-wave radiation by comparing four different locations within the simulation domain. Following the validation, the micro-scale effects of vegetation and buildings on short-wave radiation in a realistic urban environment are examined. Lastly, uncertainties related to the urban environment or input data are addressed.

This paper is structured as follows. The PALM model configuration and the radiative transfer model are explained in Section. 2.1 and Sect. 2.1.2, respectively. Initial and boundary conditions used for simulations are described in Section 2.2, followed by the domain description (Sect. 2.3), measurement description (Sect. 2.4), simulated episodes (Sect. 2.5), and experiment workflow in Section 2.7. In section 3, we present the results. Lastly, Sections 4 and 5 present the discussion and conclusion, respectively.

2 Methodology

2.1 PALM model configuration

The micro-scale simulations were performed using the PALM model system (Maronga et al., 2020) in version 25.04 (see Data availability section). The aforementioned model is a turbulence-resolving LES micro-scale meteorological model developed to support urban boundary-layer and climate research (Maronga et al., 2015, 2020). By employing the non-hydrostatic, filtered, Boussinesq-approximated incompressible Navier–Stokes equations together with a suite of specially developed components (see e.g., Maronga et al. (2020)), this numerical framework serves as a robust tool for theoretical and practical evaluation of the urban atmosphere at the street scale. Due to its modular architecture, PALM can be configured for specific applications; for example, when wind dynamics are not required, as in simulations focused solely on short-wave solar radiation, the model can be run in spin-up mode. This arrangement greatly reduces computational requirements while still enabling the evaluation and execution of a larger number of configurations and parameterisations. In this mode, the surface energy balance is solved using the Land Surface Model (LSM; Gehrke et al., 2021), Building Surface Model (BSM; Resler et al., 2017; Maronga et al., 2020), Radiative Transfer Model and Plant Canopy Model (RTM and PCM; Krč et al., 2021), with the static driver, without the need for LES. Depending on the configuration, the primary radiative forcing is provided either by a model integrated in PALM (such as RRTMG) or, as in this study, by the prescribed external forcing from the dynamic driver file. The dynamic driver values are usually obtained either from a meso-scale model such as WRF, or from measured values. As a result, any biases in the simulated short-wave radiation will be caused by driver errors, geometry effects (sky view factor), or incorrect input parameters. The present experimental setup utilises a pre-validated urban simulation domain of Dejvice, Prague (Resler et al., 2021). Micro-scale simulations were performed using the spin-up methodology, with the LSM, BSM, RTM, and MESO modules employed in this study. Furthermore, it should be noted that PALM does not explicitly resolve cloud processes; instead, their radiative impact is represented through externally specified forcing. A comprehensive description of the spin-up methodology follows below.

2.1.1 Spin-up simulations

In the context of this study, the term “spin-up” refers to the simplified operational mode of the PALM model system used to perform the primary micro-scale simulations focused on energy-balance processes, rather than to a separate pre-processing phase. The spin-up simulations constitute the primary simulations analysed herein. During this mode, the dynamic-related processes are fixed, while radiation and energy-balance processes are fully simulated. Simplification of dynamic processes can influence energy exchange on natural and building surfaces and, consequently, outgoing long-wave radiation, but it does not affect short-wave radiation, which this study focuses on. Radiation and geometric effects-such as shadings from buildings or trees, multiple reflections, and view factors-are still included in the simulation.

Surface albedo (reflectance) values are prescribed for each individual surface grid element and remain constant in time; no explicit incidence-angle-dependent albedo parameterisation is applied. On the other hand, the total effective albedo (ratio of reflected to incoming radiation) for larger areas does change in time as a result of changing solar geometry when the 3-D

radiation with multiple reflections is simulated by RTM. Furthermore, vegetation characteristics (i.e, leaf area density (LAD), canopy height, and all plant-canopy parameters) defined in the static driver are prescribed and remain constant throughout the simulations. Similarly, prescribed land-surface parameters, such as root distribution, soil moisture and temperature, and deep-soil temperature, are fixed through the model configuration. For a detailed specification of the static driver data included in this study (i.e., individual land-surface and plant-canopy input parameters), we refer to the validation study by Resler et al. (2021). The only parameter that may evolve during spin-up is soil moisture when the option *calc_soil_moisture_during_spinup* is enabled, allowing the prognostic soil-moisture equation to be solved. In the simulations analysed in this study, this option was disabled; therefore, soil moisture remained fixed throughout the simulation period. Additional sensitivity experiments with the option enabled showed no measurable impact on the simulated short-wave radiation at the vegetated HAN station for episode e5, indicating that reflected short-wave radiation was insensitive to soil moisture variations during the investigated episode.

The PALM simulation domain utilises a horizontal and vertical grid resolution of 1 m ($\Delta x = \Delta y = \Delta z = 1$ m) with the simulation domain extending 800 m in the x-direction, 500 m in the y-direction, and 100 m in the z-direction, utilising a 5 s timestep during the spin-up simulations. Regarding the simulation duration (i.e., the spin-up length), while the selected physical episodes cover 24- to 48- hour periods, the simulations for each day were initiated at 23:00 UTC (one hour prior to the target date) and lasted 23 or 46 hours, depending on the selected physical episode. This one-hour initialisation offset (starting at 23:00 UTC) was implemented to address technical constraints within the PALM/PALM-meteo framework, with no loss of critical data, since short-wave radiation is zero at midnight. PALM output data were recorded at a frequency of 600 s (10 minutes). Furthermore, the PALM-modelled irradiance values for the pyranometers were taken at the grid cell nearest to the sensors' actual locations. In the vertical direction, this translates to 1 m above ground, corresponding to the installation height of the upward- and downward-facing sensors. Consequently, the comparison with observations was performed using modelled irradiance at the sensor height rather than surface radiative fluxes. The short-wave irradiance of the sensors was modelled identically to that of actual surfaces in the RTM module of the PALM model, utilising fully 3-D radiative interactions with multiple reflections and shading by the modelled terrain and buildings, and partial attenuation by the fully resolved vegetation. More details about RTM are available in Krč et al. (2021). The identified limitation was the agreement between the modelled representation and reality, particularly regarding tree crown shapes in the input data (see Section 4.1 and Figure 8, which compares the photographed reality and the modelled representation).

2.1.2 RTM configuration

The RTM version used in this study is 4.1, which utilises a ray-tracing algorithm for handling fully 3D structures, including downward-facing faces, which differs from RTM 3.0, which operates by default on 2.5D geometry. The new localised ray-tracing parallelisation algorithm for calculating sky view factors, introduced in version 4.0, was employed. To identify all the rays affecting each grid cell, the angular discretisation algorithm (Krč et al., 2021, section 2.2) is used. The default settings are 4.5 degrees in zenith and azimuthal direction (40 zenith angles and 80 azimuth angles, resulting in a total of 3,200 possible directions). For experimental purposes, the RTM's external radiation scheme option was utilised, which uses the meso-scale model WRF's 10-minute outputs for external radiative input data (i.e., short- and long-wave downwelling radiation). Radiation

in PALM, including RTM, is computed at configured time-steps, which are typically coarser than the main model time-steps; one minute was the case in the presented simulation. At each radiation time step, the data from the external radiation inputs (10-minute WRF radiation in the presented case) were interpolated linearly in time, RTM was computed and the modelled values representing the measurement locations were exported. After the PALM simulation, the exported outputs were aggregated into hourly data (see Section 2.6).

2.2 Initial and boundary conditions

For the radiation initial and boundary conditions, the Weather Research and Forecasting (WRF) model (Skamarock et al., 2019) in versions 4.4 (WRF-CNU setup; denoted interchangeably as CNU) and 4.6.1 (WRF-FU setup, denoted interchangeably as FU) was employed. WRF is a widely used, state-of-the-art meso-scale numerical weather prediction system designed for both atmospheric research and operational forecasting. It comprises two dynamical cores, a data assimilation system, and a software architecture that supports parallel computation and system extensibility. The model serves a wide range of meteorological applications across scales, from tens of meters to thousands of kilometres, and, together with field measurements, can serve as input forcing for micro-scale simulations.

The radiative forcing used in this study is derived from two different WRF model setups: a coarse-resolution non-urban setup (WRF-CNU; 3 km horizontal resolution), and a fine-resolution urban setup (WRF-FU; 1 km horizontal resolution). The specific technical configurations for the WRF grid nesting are fully detailed in Fig. S14 in the supplementary material. Although WRF output is processed through PALM-meteo to generate a "complete" PALM dynamic driver file, the spin-up simulations employed in this study utilise only the WRF-derived short-wave and long-wave radiation fields. The remaining meteorological variables contained in the dynamic driver are not dynamically coupled to the PALM simulations and therefore do not contribute to the analysed radiative response. Both WRF simulation setups were initialised using the European Centre for Medium-Range Weather Forecasts (ECMWF) atmospheric reanalysis, ERA5 data (Hersbach et al., 2020). A comparative overview of the physics schemes for both WRF configurations is summarised in Table 1. Typically, the main WRF output files contain data at 1-hour intervals. However, when addressing radiation modelling in the context of changes in solar irradiance and the likelihood of cloud development and movement, it is preferable to configure WRF to generate auxiliary output files containing only radiation-related variables at a finer temporal resolution (e.g., 10 minutes). Furthermore, the WRF files for the PALM-meteo (the preprocessor of meso-scale meteorology which generates the PALM dynamic driver; see Krč et al., 2025) need to contain short-wave and long-wave horizontal irradiance (marked in WRF as downward radiation); the diffuse component of the short-wave horizontal irradiance is optional. If this component is absent, it is skipped during dynamic driver preprocessing, and the PALM radiation module uses its internal estimate of the direct-to-diffuse ratio. When utilising a high-resolution model such as PALM, it is preferable to provide high-quality input data (Radović et al., 2024). Hence, for radiation, this study uses 10-minute WRF radiation data to drive the PALM model. A schematic representation of the modelling chain showing the sequential data flow from the meso-scale WRF forcing through the PALM-meteo pre-processor, the dynamic driver to PALM/RTM, is presented in Appendix B.

Table 1. WRF parametrisation schemes utilized in the experiment.

Physics Scheme	WRF-CNU[1]	WRF-FU[2]
Planetary Boundary Layer	MYNN Level 2.5 (Nakanishi and Niino, 2009)	Bougeault–Lacarrere Scheme (BouLac; Bougeault and Lacarrere, 1989)
Urban Physics	0 (disabled)	BEP+BEM (Martilli et al., 2002; Salamanca and Martilli, 2009)
Long-wave radiation	RRTMG (Iacono et al., 2008)	RRTMG (Iacono et al., 2008)
Short-wave radiation	RRTMG (Iacono et al., 2008)	RRTMG (Iacono et al., 2008)
Surface layer	Revised MM5 Scheme (Jimenez et al., 2012)	Revised MM5 Scheme (Jimenez et al., 2012)
Land Surface	Unified Noah Land Surface Model (Tewari et al., 2004)	Unified Noah Land Surface Model (Tewari et al., 2004)
Microphysics	Thompson (Thompson et al., 2008)	Thompson (Thompson et al., 2008)

[1] Coarse-resolution non-urban setup–WRF-CNU (3 km horizontal resolution)

[2] Fine-resolution urban setup–WRF-FU (1 km horizontal resolution)

2.3 Study area description

The study area is located in Dejvice, a district of Prague, the capital of the Czech Republic. As presented in Holtanová et al. (2025), Prague is in a temperate continental climate zone.

The average annual air temperature recorded at the meteorological station Praha-Klementinum (WMO ID 11515, located in the city centre) was 11.5 $^{\circ}\mathrm{C}$, according to the WMO's Climatological Standard Normal for 1991–2020. The mean air temperature in July, typically the warmest month, was 21.6 $^{\circ}\mathrm{C}$. The coldest month, with a temperature of 1.8 $^{\circ}\mathrm{C}$, is typically January. Average annual precipitation is 453.9 mm, and mean monthly sunshine hours range from 46.2 (December) to 229.1 (July).

There are four major types of built-up areas in Dejvice (Fig. 1) with the following Local Climate Zone (LCZ; Stewart and Oke, 2012) classification: 1) historical residential areas in south-east, classified as LCZ 2 Compact midrise, 2) a combination of old and new buildings with a variety of other urban components (west and north-west), predominantly classified as LCZ 5 Open midrise, 3) a residential area with green gardens (north-east) that corresponds to LCZ 6 Open lowrise, and 4) lightly wooded landscape of deciduous trees, with a grass sublayer (LCZ B Scattered trees; more precisely in the case of Hanspaulka (HAN) observational station (see Fig. 1), the transitional class LCZ $\mathrm{B_D}$).

2.4 Measurement campaign and observational dataset

Measurement locations (see Fig. 1) were situated in the north-west of Dejvice, mainly in the Czech Technical University campus. There were two calibrated stations, each producing 10-minute averages for two years (2017–2018). At the end of

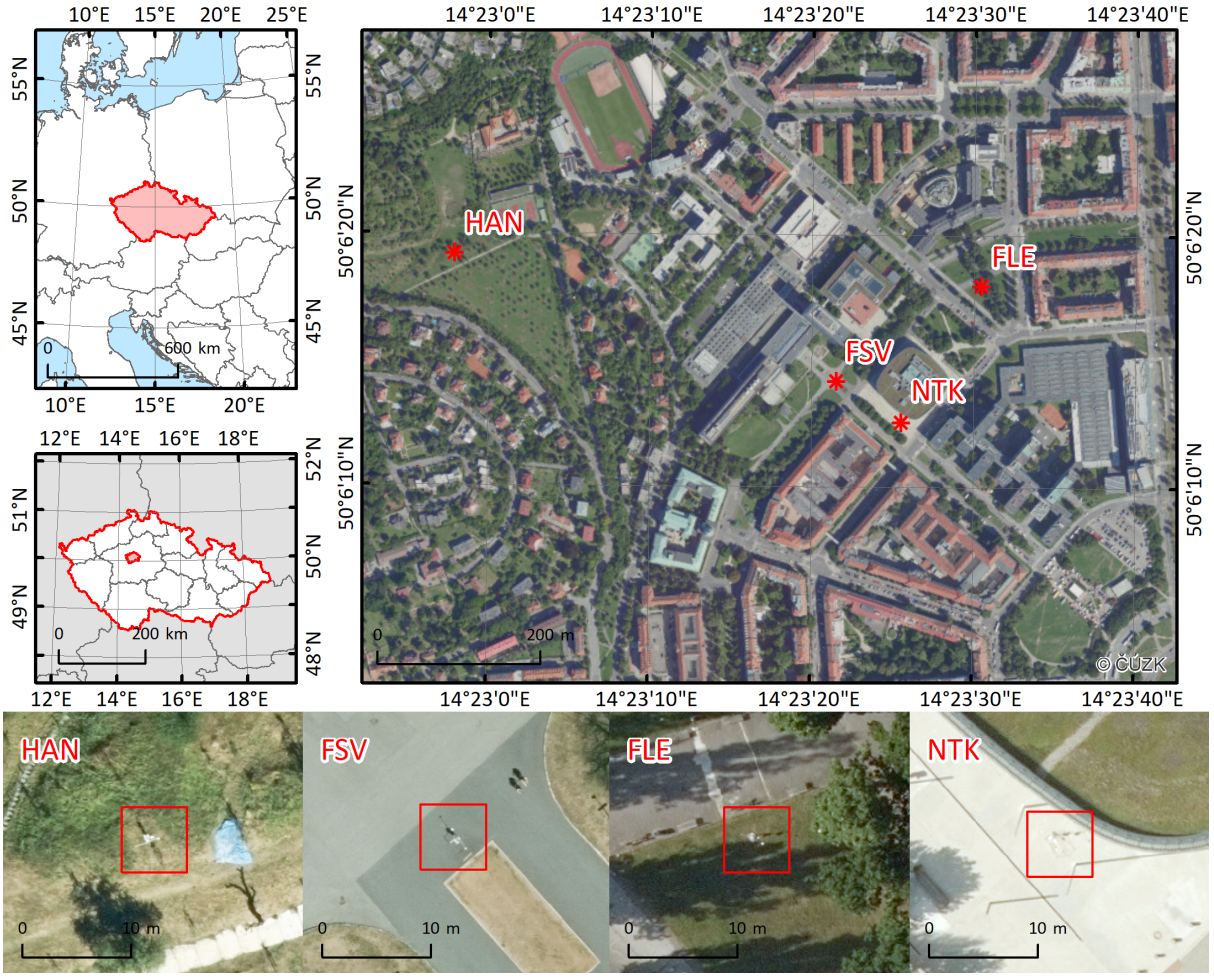

Figure 1. The position of the domain in Central Europe (top left) and the Czech Republic (middle left). Red stars indicate measurement location. The orthophotography on the top right map was provided by the Czech Cadastral Office © via the web map service. The bottom figures represent the individual station locations (red squares) in 2017 and 2018. The orthophotographs for year-specific locations were provided by the Prague Institute of Planning and Development (IPR) ©. Note that IPR orthophotographs are from a perspective view.

the year 2017, both stations were moved to a new position (four locations in total; see Table 2) (Jura et al., 2018). The first location, opened in 2017, was situated on the asphalt surface (FSV) and was primarily influenced by the surrounding buildings. The effect of the plant canopy, distanced ≈20 m with an approximate crown perimeter of 2 m, was negligible in most cases.
240 The second position in 2017 was in a public orchard with fruit trees (HAN). The station surroundings were affected during the vegetation season by various grass heights (0.2–1.0 m) and available soil moisture. The majority of fruit trees were lower than 4 m and were distanced more than 5 m from the measurement location. The third location, first in 2018, was in a small park known as Fleming Square (FLE). The station was situated on a homogeneous grass surface and was significantly impacted

by neighbouring trees. The last location (NTK), second in 2018, was situated on light grey coloured concrete, between the National Technical Library building and a tree alley (height 8–10 m) on the south-west. An additional note pertains to the curved glassy walls of the neighbouring library, which, under specific conditions, can reflect incoming short-wave radiation.

Table 2. Characteristics of the four measurement locations in Prague-Dejvice used in this study. The table lists the station coordinates, year of installation, surface albedo, and the sky view factor (Sky VF), obstacle view factor (Obstacle VF), and tree view factor (Tree VF) derived from the three-dimensional urban geometry in the PALM model.

Name	Coordinates (latitude, longitude)	Year	Surface albedo	Sky VF	Obstacle VF	Tree Vf
FLE	50.1049783 N, 14.3917394 E	2017	0.173	63.52 %	0.96 %	35.52 %
NTK	50.1034739 N, 14.3905364 E	2017	0.247	69.39 %	29.60 %	1.01 %
FSV	50.1039264 N, 14.3892972 E	2018	0.120	88.10 %	10.56 %	1.34 %
HAN	50.1052408 N, 14.3825917 E	2018	0.170	92.47 %	0.89 %	6.63 %

Each measurement station was equipped with several sensors: two RVT 11 for air temperature and relative humidity (at heights of 0.3 and 2.0 m), three Pt_{100} for soil temperature (at various depths), a "Tlusťák W2" anemometer for wind speed and direction, and two Kipp&Zonen CMP3 pyranometers with the spectral range from 300 to 2,800 nm for incoming and reflected solar radiation. The pyranometer's interval covers most of the short-wave radiation spectrum, although not the entire spectrum; in the following text, its results as a short-wave radiation measurement will be considered. Details about sensors are available in Table 3 or Jura et al. (2018).

In addition to the dedicated observation stations described above, meteorological observations-particularly short-wave radiation measurements-from the Czech Hydrometeorological Institute (CHMI) stations Praha-Libuš (WMO ID 11520) and Praha-Karlov (WMO ID 11519) were also employed. The Praha-Libuš station (50.0077° N, 14.4467° E; 302 m a.s.l.), located in the southern part of Prague, is the reference aerological and meteorological observatory. Owing to its long-term operational record and high-quality measurements, it serves as one of the principal reference stations for meteorological measurements in the Prague region. The Praha-Karlov station (50.0691° N, 14.4276° E; 261 m a.s.l.) is situated closer to the central urban area of Prague and represents conditions typical of a more densely urbanised environment. In this study, both stations provide independent short-wave radiation observations used to evaluate the radiative conditions associated with the analysed episodes. While these stations could, in principle, provide observational radiation forcing data for the PALM model, in the present study, they were used exclusively as out-of-domain reference evaluation stations, rather than as direct model forcing.

Table 3. Sensors on the measuring stations and their technical parameters. Surface albedo values were calculated using measurements in Jura et al. (2018).

Sensor	Variables	Range	Typical accuracy	Resolution
Kipp&Zonen CMP3[1]	global radiation (income)	0–2,000 $\mathrm{Wm^{-2}}$	$\pm$ 5 %	24 to 32 $\mu\mathrm{VW^{-1}m^2}$
	global radiation (reflected)	0–2,000 $\mathrm{Wm^{-2}}$	$\pm$ 5 %	24 to 32 $\mu\mathrm{VW^{-1}m^2}$
RVT 11[2]	air temperature	-30 to 50 °C	$\pm$0.3 °C	0.001 °C
	relative humidity	0–100 %	$\pm$1.8 %	0.1 %
Tlusťák W2[3]	wind direction	0–360 °	10 °	1 °
	wind speed	0,7–30 $\mathrm{ms^{-1}}$	$\pm$ 4 %	0.1 $\mathrm{ms^{-1}}$
Pt_{100}[4]	soil temperature	-50 to 120 °C	$\pm$0.23 °C for max 40 °C	0 °C

[1] OTT HydroMet B.V., Netherlands; [2] SENSIRION AG, Switzerland; [3] Tlusťák TM, Czech Republic; [4] SENSIRION AG, Switzerland.

2.5 Simulation episodes and meteorological conditions

Atmospheric conditions with no cloud cover, or the so-called "clear-sky" days, characterised by a smooth, parabolic-shaped curve, are an ideal testbed for evaluating radiation physics in micro-scale models like PALM, thanks to a high confidence in the incoming solar radiation. Nevertheless, high-solar-irradiance weather conditions with a completely cloud-free sky are relatively rare; more realistic conditions involve heterogeneous variations of thin cirrus, scattered cumulus, or cloud fragments. To cover a series of typical summer heat wave periods and the corresponding atmospheric radiation regimes, a total of 16 episodes with various types of synoptic and cloud cover conditions during the summers of 2017 and 2018 were selected for model evaluation. Since the chosen episodes differ in cloud cover, they are categorised into two groups: predominantly cloud-free episodes, referred to as "clear-sky" (i.e., clear-sky proxies), and episodes with pronounced cloudiness, referred to as "non-clear-sky" episodes. The selection of "clear-sky" episodes was based on a qualitative inspection of the observed incoming short-wave radiation to identify periods exhibiting a continuous, smooth, "bell-shaped" diurnal curve. To formalise this for future protocols, we define such episodes as days during which the measured short-wave radiation does not deviate from the theoretical clear-sky envelope, indicating the absence of transient cloud shading. For "non-clear-sky" episodes, we selected days during which the observed short-wave radiation showed high-frequency fluctuations relative to the potential clear-sky maximum. Simulation episodes cover a range of large-scale weather systems and fronts crossing Prague (e.g., cyclonic and anticyclonic), providing a realistic set of meteorological conditions (see Table S1). In addition, the maximum solar elevation was calculated for each of the simulation episodes, ranging from $44.41°$ during the autumn to $63.37°$ at the summer peak. Six of the 16 episodes (e1–e6) serve as a sample for the direct WRF setup-to-setup intercomparison (i.e., CNU vs. FU). To further validate the WRF-FU's setup generalisability and transferability and to deliver a more robust statistical evaluation, the analysis was extended to 10 additional episodes (e7–e16) simulated using the WRF-FU setup only. Comprehensive details on the simulation episodes, maximum solar elevation, cloud conditions, and associated WRF driving configurations are provided in Table 4.

Table 4. Overview of simulation episodes, maximum solar elevation, cloud conditions, and WRF configurations used in the study. The six common episodes (e1–e6) used for direct comparison were simulated with both the Coarse No Urban (WRF-CNU) and Fine Urban (WRF-FU) configurations, while the additional episodes (e7–e16) were simulated only with the FU configuration.

Episode	Date	Maximum solar elevation	Cloud conditions	Category
Common episodes				
e1	19–20/06/2017	63.35° and 63.37°	clear-sky	Common
e2	19/07/2017	60.93°	clear-sky	Common
e3	07/08/2017	56.57°	clear-sky	Common
e4	30/06/2018	63.16°	clear-sky	Common
e5	02–03/07/2018	63.04° and 62.96°	clear-sky	Common
e6	11–12/09/2018	44.79° and 44.41°	clear-sky	Common
Additional episodes				
e7	09/06/2017	62.80°	clear-sky	FU-only
e8	11/06/2017	62.96°	clear-sky	FU-only
e9	07/07/2017	62.61°	non-clear-sky	FU-only
e10	16/06/2018	63.26°	non-clear-sky	FU-only
e11	07/07/2018	62.61°	clear-sky	FU-only
e12	21/07/2018	60.56°	non-clear-sky	FU-only
e13	24/07/2018	59.97°	clear-sky	FU-only
e14	01/08/2018	58.15°	clear-sky	FU-only
e15	17/08/2018	53.60°	clear-sky	FU-only
e16	20/08/2018	52.63°	clear-sky	FU-only

2.6 PALM output and observation data processing

The subsequent evaluation is designed to quantify the influence of WRF mesoscale driving data on PALM-simulated incoming and outgoing short-wave radiation and to identify the conditions under which PALM accurately reproduces observed radiative processes or exhibits systematic biases. To achieve this, PALM outputs from two WRF configurations (CNU and FU) were compared with observations using complementary statistical and radiative-process-oriented analyses.

PALM output data are produced every 60 s relative to the simulation start. For each simulation episode, incoming and outgoing short-wave radiation fluxes (SWin and SWout) are extracted at the locations of the observation stations and averaged into hourly mean values. Similarly, measurements (recorded at 10 min intervals) were aggregated into hourly means. The obtained datasets for both variables are further distinguished by WRF driver (CNU and FU) and station. All subsequent analyses (statistical metrics, summary mean bias and root mean square error heatmaps, and scatter plots) are derived from these model/observation hourly data. The evaluation was designed to address several aspects of micro-scale model performance. First,

the overall impact of the WRF driving configurations on the PALM-simulated short-wave radiation was assessed. Second, the ability of PALM to reproduce the magnitude and temporal variability of observed radiative fluxes was evaluated. Third, the PALM's capability to resolve local radiative processes associated with urban morphology and vegetation was examined. Finally, the robustness of PALM under non-clear-sky atmospheric conditions was investigated.

Firstly, the overall model performance was evaluated using absolute and relative differences between modelled and observed values. Absolute differences provide a direct measure of the magnitude of model errors. Relative differences are expressed as percentages relative to the observed values and are used to assess the magnitude of model deviations independent of absolute radiation intensity. These metrics were calculated for each station, radiation variable, simulation episode, and WRF driving configuration, and presented to facilitate comparisons between stations, sky conditions, and driving-data setups.

To further quantify model performance, we employ a multi-level evaluation procedure. First, we calculate overall and station-specific Mean Bias Error (MBE) and Root Mean Square Error (RMSE) using twofold averaging: first, per episode (single episode–station–variable–WRF driver value), and then averaging across all episodes. These are visualised as summary heatmaps. Second, point-by-point comparisons between modelled and observed values are presented in scatter plots, where each point represents an hourly value at a specific station and WRF driver. Performance is further assessed using statistical metrics including Pearson's correlation coefficient (r), coefficient of determination (R^2), Spearman's ρ, Kendall's τ, and Willmott's index of agreement (d). Results are stratified by WRF driver (CNU vs FU), sky conditions (clear-sky vs non-clear-sky episodes), and station type (urban vs vegetated).

In addition to bulk statistical evaluation, we quantitatively analyse diurnal cycles of SWin and SWout. This approach allows the assessment of the model's ability to capture key radiative processes such as shading patterns induced by urban morphology, the influence of surface characteristics (e.g., vegetation), and performance under complex cloudy conditions. Specific episodes are selected to highlight these aspects: clear-sky cases for shading and surface representation issues, and non-clear-sky episodes for cloud–radiation interaction.

3 Results

The outcome of our simulations emphasises the link between meso-scale driving data and PALM micro-scale radiation process modelling. As shown in Radović et al. (2024), PALM performance largely depends on the quality of the forcing fields, whose features (e.g., general structure and biases) propagate into the micro-scale simulation, further affecting modelled variables. In order to describe the particular impact of forcing fields on short-wave radiative fluxes, PALM's response to the two distinct WRF model setups is quantified. The general pattern between PALM and the corresponding observed radiation-related variables is identified (Fig. 3 and Fig. 4). To target differences and patterns between modelled and observed values, the data are clustered by WRF driver, cloud conditions, variables, and stations. The data are further processed, and the direction and magnitude of errors are quantified (Fig. 2).

3.1 An overall view of the simulations

The influence of sky conditions and the configuration of driving data on PALM simulations is reflected in both absolute and relative metrics defined in Supplement Section 1 (see the differences in Tab. 5). Under non-clear-sky episodes (see, e.g., column Non-clear (FU) in Tab. 5), and for all stations considered, SWin exhibits consistently large errors, with average absolute differences above 80 Wm^{-2} and average relative differences exceeding 100 $\%$. The strongest degradation occurs at the NTK station, with a relative difference of 276.6 $\%$, and at the FLE station, with an increase of over 100 $\%$. These are station-specific anomalies that are not observed at the other two locations. The modelling of SWout is only slightly affected, as the increase in discrepancies is not substantial, except at the NTK station. On the other hand, PALM's fidelity improves for the clear-sky scenario simulated with the FU configuration, with both examined variables exhibiting comparatively small biases. However, the HAN station exhibits large relative and absolute differences, a pattern that holds across all sky conditions and driving data configurations. A more detailed analysis of the HAN station is presented in Section 3.2.2. The metrics quantifying the impact of the WRF configurations on SWin indicate that the FU outperforms the CNU, as the overall absolute difference decreases from 67.9 Wm^{-2} (CNU) to 39.8 Wm^{-2} (FU; corresponding to a reduction of roughly 40 $\%$). Compared with SWin, WRF-FU improves SWout only at urban stations (FSV and NTK), whereas biases persist at vegetated sites (HAN and FLE), resulting in similar overall relative and absolute differences.

Table 5. Absolute and relative differences ($\%$) for PALM-simulated incoming (SWin) and outgoing (SWout) short-wave radiation, evaluated across four measurement stations (FSV, NTK, HAN, and FLE). The results are categorised by sky conditions (Clear vs. Non-clear) and by WRF driving configurations (FU and CNU; see Table 4).

Station	Variable	Non-clear (FU)	Clear (FU)	Common (CNU)	Common (FU)
FSV	SWin	74.0 (19.3 $\%$)	37.8 (-2.5 $\%$)	78.2 (1.6 $\%$)	43.4 (1.3 $\%$)
	SWout	10.7 (4.3 $\%$)	10.6 (-10.4 $\%$)	15.6 (-16.8 $\%$)	11.6 (-11.7 $\%$)
NTK	SWin	163.8 (276.6 $\%$)	38.0 (17.0 $\%$)	81.2 (1.2 $\%$)	33.5 (10.2 $\%$)
	SWout	37.7 (163.3 $\%$)	14.3 (-2.1 $\%$)	28.2 (-15.7 $\%$)	16.2 (-7.6 $\%$)
HAN	SWin	59.2 (24.0 $\%$)	31.5 (9.0 $\%$)	53.2 (-4.7 $\%$)	31.9 (5.1 $\%$)
	SWout	53.6 (-38.6 $\%$)	56.8 (-52.9 $\%$)	56.8 (-52.6 $\%$)	56.5 (-52.9 $\%$)
FLE	SWin	96.0 (110.6 $\%$)	56.7 (-1.3 $\%$)	58.9 (9.7 $\%$)	50.3 (-2.2 $\%$)
	SWout	15.0 (1.9 $\%$)	12.2 (-3.6 $\%$)	11.7 (-3.1 $\%$)	11.6 (-4.1 $\%$)
Overall	SWin	87.7 (107.6 $\%$)	39.5 (5.0 $\%$)	67.9 (2.0 $\%$)	39.8 (3.6 $\%$)
	SWout	30.2 (32.7 $\%$)	25.8 (-20.5 $\%$)	28.1 (-22.3 $\%$)	24.0 (-19.1 $\%$)

Given the performance metrics indicated by the Person's correlation coefficient r, Spearman's ρ, and Willmott's index of agreement d, the timing and magnitude of the modelled and observed values for SWin show a satisfactory agreement for both of the driving data configurations considered ($\mathrm{r} \approx 0.985$, $\rho \approx 0.984$, $\mathrm{d} \geq 0.980$; see Tab. 6; metrics are defined in Supplement Section 1). An evaluation of all indicators, however, suggests that the FU configuration performs somewhat better than the

CNU setup, particularly at urban stations (i.e., FSV and NTK). Outgoing short-wave radiation (SWout) shows a greater spread in performance metrics than SWin. There is a pronounced systematic bias in SWout at the HAN site, as indicated by low correlation and agreement metrics, and the strongly negative coefficient of determination ($R^2 \approx -1.4$). This bias is consistent across the full analysis and in every tested configuration, indicating that the dominant source of error lies in the surface representation at HAN rather than in the driving data forcings alone. When examining PALM's performance under different sky conditions (see Tab. 6; FU Clear-Sky and FU Non-Clear-Sky), the contrast is clear and expected: the model reproduces SWin with high accuracy during clear-sky periods. This level of accuracy is not achieved in episodes with cloud cover, where performance metrics degrade noticeably for both variables. PALM's overall performance shows that SWin is represented with high fidelity under clear-sky conditions when using the updated FU-driving data. Although PALM's simulation of SWout is not poor, a clear deterioration in the evaluation metrics is evident, particularly at vegetated sites. Under conditions other than clear skies, PALM struggles to model radiation, and its performance remains inconsistent.

Table 6. Statistical performance metrics for PALM-simulated incoming (SWin) and outgoing (SWout) short-wave radiation across four measurement stations (FSV, NTK, HAN, and FLE). The upper part refers to the PALM outputs driven by the WRF-CNU and WRF-FU configurations during clear-sky conditions and common episodes, and the bottom section compares PALM outputs driven by the WRF-FU configuration during clear-sky and non-clear-sky episodes (see Table 4). Metrics include Pearson correlation (r), coefficient of determination (R^2), Spearman's rho (ρ), Kendall's tau (τ), and Willmott's index of agreement (d). The formulas used for the statistical analysis are described in the supplementary material, under the metrics defined in Supplement Section 1.

Station	Variable	CNU Common Clear-Sky					FU Common Clear-Sky				
		r	R^2	Spearman's ρ	Kendall's τ	d	r	R^2	Spearman's ρ	Kendall's τ	d
FSV	SWin	0.993	0.922	0.992	0.934	0.980	0.987	0.966	0.989	0.932	0.992
	SWout	0.981	0.774	0.982	0.891	0.939	0.963	0.830	0.968	0.854	0.957
NTK	SWin	0.996	0.928	0.995	0.951	0.978	0.994	0.985	0.989	0.913	0.995
	SWout	0.992	0.842	0.979	0.889	0.955	0.990	0.941	0.973	0.874	0.985
HAN	SWin	0.983	0.939	0.976	0.867	0.987	0.981	0.963	0.979	0.882	0.994
	SWout	0.826	-1.332	0.866	0.685	0.625	0.730	-1.438	0.802	0.626	0.620
FLE	SWin	0.984	0.947	0.987	0.913	0.983	0.978	0.950	0.981	0.890	0.988
	SWout	0.982	0.909	0.980	0.880	0.963	0.970	0.913	0.973	0.856	0.977
Overall	SWin	0.989	0.934	0.988	0.916	0.982	0.985	0.966	0.984	0.904	0.992
	SWout	0.945	0.298	0.952	0.836	0.870	0.913	0.312	0.929	0.802	0.885

Station	Variable	FU Clear-Sky					FU Non-Clear-Sky				
		r	R^2	Spearman's ρ	Kendall's τ	d	r	R^2	Spearman's ρ	Kendall's τ	d
FSV	SWin	0.989	0.974	0.991	0.926	0.993	0.957	0.889	0.943	0.818	0.972
	SWout	0.971	0.847	0.976	0.860	0.955	0.950	0.859	0.904	0.742	0.960
NTK	SWin	0.993	0.980	0.989	0.909	0.994	0.886	0.676	0.900	0.733	0.904
	SWout	0.990	0.952	0.974	0.869	0.987	0.881	0.711	0.864	0.692	0.901
HAN	SWin	0.988	0.971	0.985	0.898	0.994	0.960	0.882	0.953	0.857	0.971
	SWout	0.493	-1.806	0.698	0.526	0.574	0.568	-0.804	0.625	0.450	0.604
FLE	SWin	0.973	0.944	0.982	0.893	0.986	0.938	0.872	0.847	0.667	0.967
	SWout	0.966	0.915	0.970	0.853	0.977	0.940	0.881	0.786	0.590	0.967
Overall	SWin	0.986	0.967	0.987	0.907	0.992	0.935	0.830	0.911	0.769	0.954
	SWout	0.855	0.227	0.904	0.777	0.873	0.935	0.412	0.795	0.618	0.858

Fig. 2 illustrates PALM performance and accuracy through the MBE and RMSE error distributions for both incoming and reflected short-wave radiation across four stations. The arrangement in Fig. 2 is to isolate the impact of driving data configurations and sky conditions on the model's performance. In the CNU-driven setup, the incoming short-wave radiation (SWin-CNU) is underestimated across all evaluated stations. The negative biases span from $-13\ \mathrm{Wm}^{-2}$ to $-46\ \mathrm{Wm}^{-2}$, most pronounced at the FSV and NTK stations (Fig. 2a). Conversely, for SWin-FU, the MBE values are significantly reduced, approaching 0, and at the HAN and FLE stations, they become slightly positive. For outgoing short-wave radiation, both SWout-CNU and SWout-FU exhibit negative biases, which are reduced when using the FU configuration. The only exception is the HAN station, where both setups show a strong negative bias greater than $-30\ \mathrm{Wm}^{-2}$. This bias pattern is further supported by the RMSE values (Fig. 2d), which decrease for the FU configuration for both incoming and outgoing short-wave radiation, although the reduction is less pronounced for the outgoing component.

SWin-FU biases (Fig. 2b) display a site-specific performance pattern comparable to that in Fig. 2a, with negative biases at urban stations (FSV and NTK) and positive biases at vegetated stations (HAN and FLE). SWout MBEs are generally small, except for the pronounced negative bias at the HAN station ($\approx -60\ \mathrm{Wm}^{-2}$), which remains evident and aligns with earlier analyses. The RMSE values are generally moderate; however, for SWout at the HAN station, they are notably higher than at the other stations. Finally, under non-clear-sky conditions, the model performance degrades notably, as indicated by large MBE and RMSE values, particularly for SWin (Fig. 2c,d). In the case of SWin, MBEs indicate model overestimation, with the highest value exceeding $120\ \mathrm{Wm}^{-2}$ at the NTK station. SWout biases are negative, except for the NTK station, which has a positive bias.

To separate the effect of the driving model setup on the PALM-simulated short-wave radiation, we perform a direct, point-by-point comparison, as shown in Figure 3 and Figure 4. Firstly, in the CNU-driven PALM simulations, SWin is consistently and systematically underestimated for irradiance values exceeding $600\ \mathrm{Wm}^{-2}$ (see Fig. 3a). This deviation is evident in the relatively large MBE and RMSE values of $-32.05\ \mathrm{Wm}^{-2}$ and $62.21\ \mathrm{Wm}^{-2}$, respectively. The consistent underestimation suggests that the deficiencies likely stem from the WRF-CNU driving setup and cannot be fully mitigated by PALM's high-resolution local radiative transfer calculations. In contrast, a clear improvement is observed for the WRF-FU-driven PALM simulations, in which the MBE is reduced by roughly one order of magnitude and the RMSE decreases by about 30 % compared to the CNU-driven PALM simulations (see Fig. 3b). However, the FU-based outputs at radiation levels below $300\ \mathrm{Wm}^{-2}$ show a slight spread around the 1:1 line. A noticeable deterioration in PALM's performance (also for the FU-based outputs) is evident for outgoing short-wave radiation, as illustrated in Figure 4. An initial assessment common to both configurations is a systematic underestimation of outgoing short-wave radiation, which is somewhat more pronounced when using the CNU driver. This underestimation results in a negative bias of $-16.15\ \mathrm{Wm}^{-2}$ for CNU and $-12.61\ \mathrm{Wm}^{-2}$ for the FU configuration, corresponding to an approximate reduction of 22 % in favour of the FU setup. As indicated by the RMSE values, PALM's predictions remain moderately accurate, though slightly improved in the FU configuration. Furthermore, the evaluated stations exhibit more variability for outgoing radiation. For instance, FLE (blue) and NTK (purple) align relatively well with the observations (Fig. 4b), whereas the HAN (green) station exhibits significant deviations and has the poorest correspondence (Fig. 4a,b). Although the results show that the FU driver reduces bias relative to the CNU, discrepancies with observations remain relatively high. It

implies that the model's inadequate representation of surfaces near problematic sites (i.e., HAN) influences reflected radiation and is the primary cause of these biases.

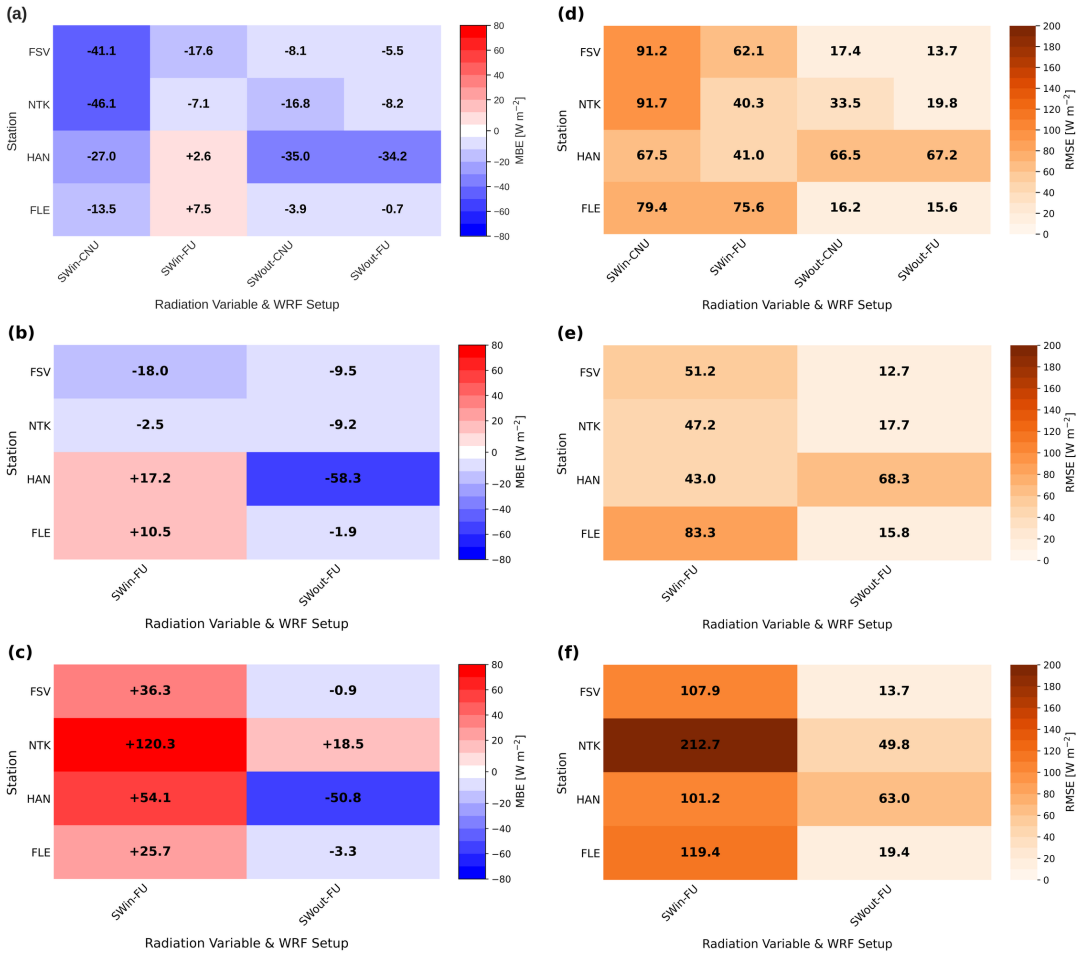

Figure 2. Summary Mean Bias Errors (MBE; a–c) and Root Mean Square Errors (RMSE; d–f) of short-wave incoming (SWin) and short-wave outgoing (SWout) radiation across 4 observational stations (FSV, NTK, HAN, and FLE) and different WRF driving data setups. Each cell contains the error averaged over the corresponding episode selection for a specific variable, observational station, and WRF model driving setup. Panels (a) and (d) correspond to the common simulated episodes driven by both CNU and FU WRF model setups, panels (b) and (e) refer to the clear-sky FU WRF model setup, while non-clear-sky episodes with the FU WRF model setup are depicted on panels (c) and (f). The colour bars represent the magnitude of the MBE and RMSE values in $\mathrm{W m^{-2}}$.

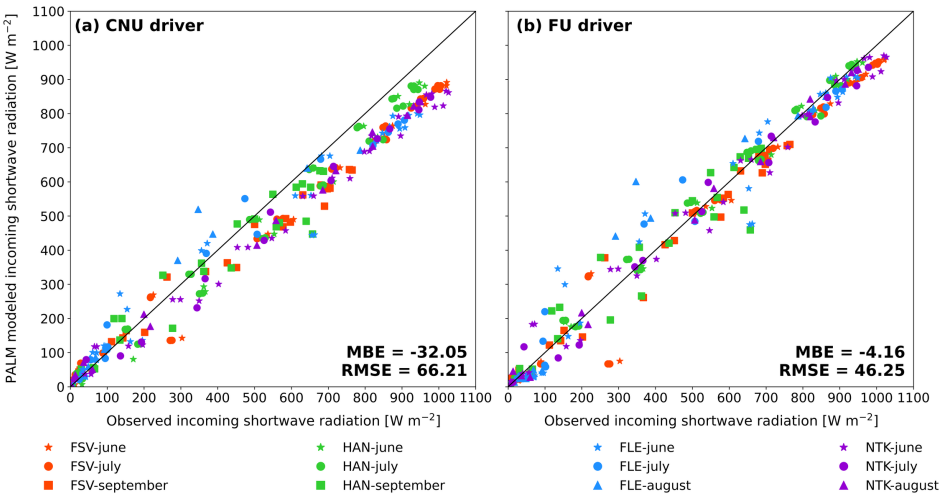

Figure 3. Scatter plots of incoming short-wave radiation for all common simulated episodes (e1–e6) and all measuring stations for the Coarse No Urban (CNU; a) and Fine Urban (FU; b) WRF-driving setup. Colours represent individual stations (FSV–red, HAN–green, FLE–blue, and NTK–purple) while marker shapes represent months of the simulated episodes (star–June, circle–July, triangle–August, and square–September). The summary Mean Bias Error (MBE) and Root Mean Square Error (RMSE) depict PALM's performance compared with observations.

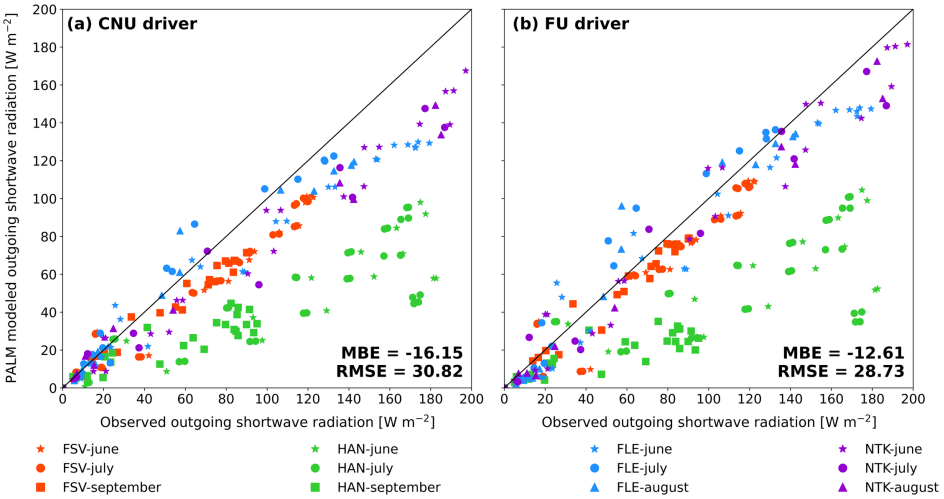

Figure 4. Scatter plots of outgoing short-wave radiation for all common simulated episodes (e1–e6) and all measuring stations for the Coarse No Urban (CNU; a) and Fine Urban (FU; b) WRF-driving setup. Colours represent individual stations (FSV–red, HAN–green, FLE–blue, and NTK–purple) while marker shapes represent months of the simulated episodes (star–June, circle–July, triangle–August, and square–September). The summary Mean Bias Error (MBE) and Root Mean Square Error (RMSE) depict PALM's performance compared with observations.

3.2 Daily cycles of incoming and outgoing short-wave radiation

Addressing the main model outputs through diurnal cycles of incoming and outgoing short-wave radiation components is a well-established benchmark for testing the overall fidelity of micro-scale models. The significance of urban meteorology studies, in particular, is underscored by the ability to capture the relationship between the moving Sun and surrounding physical objects, radiation intensity, surface albedos, and the integration of dynamic driver data. Although significant, statistical summaries cannot fully capture the specifics of the model's radiative process treatment (e.g., resolving morning and afternoon shading patterns, midday radiation intensity offsets or magnitude discrepancies, location-specific sensitivities, surface-type biases). Hence, the following subsections are organised into three complementary evaluations that demonstrate the model's fidelity (Section 3.2.1), reveal instances where the performance degradation is most clearly evident (Sections 3.2.2), and validate the model's predictive skills under more complex radiative regimes (Section 3.2.3).

3.2.1 PALM's fidelity in reproducing diurnal shading patterns

The ability to resolve three-dimensional radiative interactions, including shading patterns within a local urban environment, is a key distinguishing feature of high-resolution models such as PALM, compared with coarser, less extensive meteorological models (e.g., meso-scale or diagnostic models). The direct effect of heterogeneous urban morphology (i.e., building, street canyon, and vegetation patterns) on incoming short-wave radiation is most apparent for small solar elevation angles during sunrise and sunset. As seen from the Fig. 5, the driving model's deficiencies are evident in its inability to accurately capture the shading effects imposed on incoming solar radiation during early morning and late afternoon, whereas PALM reproduces the observed SWin profile shape with high accuracy. One notable improvement occurs during maximum solar irradiance, when the FU-driven simulation fully reproduces the SWin amplitude. In contrast, the CNU-driven setup systematically underestimates the observed solar-noon peak. This enhancement is evident at the urban NTK station, where the FU-WRF simulation shows a deficit of about 80–100 Wm^{-2}, while the CNU-WRF simulation shows an even greater deficit relative to the observed values. The SWout is simulated reasonably well by both drivers, with a similar diurnal pattern of underestimating the reflected radiation throughout the day. Although the FU-driven SWout increases minimally throughout the day, it remains consistently higher than the CNU-driven simulation and matches more closely the observed values.

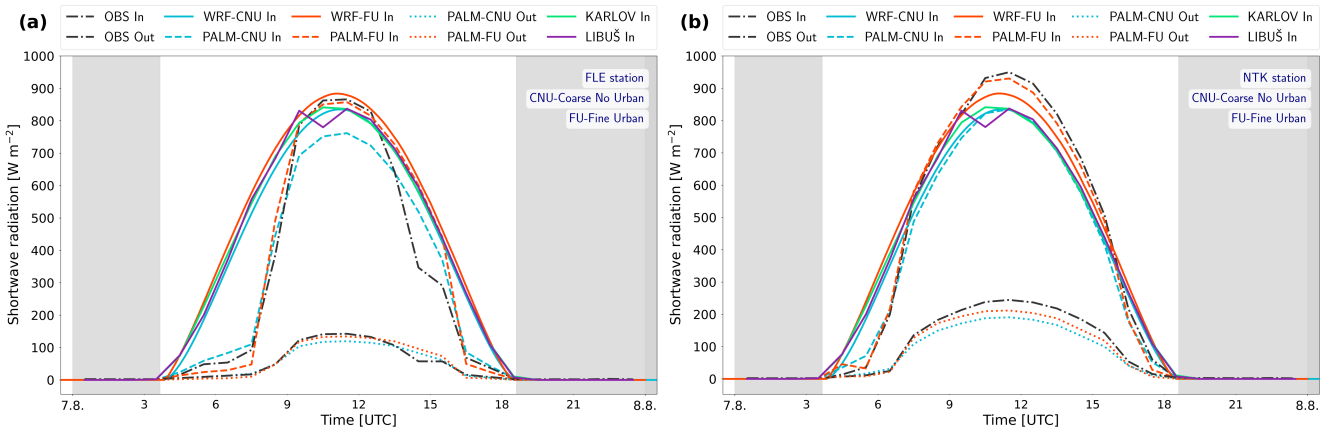

Figure 5. The comparison of observed hourly averages of incoming (In) and outgoing (Out) short-wave radiation for the e6 episode at the stations FLE (a) and NTK (b), with PALM model outputs for both WRF configurations. Additional lines represent the raw WRF outputs, Coarse No Urban (WRF-CNU), and Fine Urban (WRF-FU), and measurements from professional meteorological stations in Karlov and Libuš.

3.2.2 Vegetation effects and midday underestimation

Vegetation modulates both the incoming and outgoing short-wave radiation through processes such as absorption, reflection, and scattering. This effect is clearly captured during episode e5. As shown in Fig. 6a, the incorrectly parameterised grass cover in the PALM's static driver at the HAN station translated directly to the SWout data output by the micro-scale simulation for both WRF driving configurations. The influence of site-specific variability on SWout modelling is evident in the contrasting behaviour of PALM-simulated SWout at the urban FSV station, where both PALM setups reproduced in situ measurements, although the CNU-driven configuration performed slightly worse than the FU. During midday, the magnitude of the PALM-modelled reflected radiation drops below 100 Wm^{-2}, which is inconsistent with observations that show values between 180 and 200 Wm^{-2}. These qualitatively identified discrepancies in the SWout are evident in other analyses, where the HAN station shows the worst quantitative performance, as indicated by high MBE and RMSE values along with other supporting statistical indicators (see e.g., Figs. 2 and 4, or Tabs. 5 and 6). Another discrepancy of PALM is the midday underestimation of SWin observed at the urban FSV station. Across both WRF forcing configurations, PALM underestimates the incoming short-wave radiation, although this offset is moderately attenuated by PALM-FU downscaling.

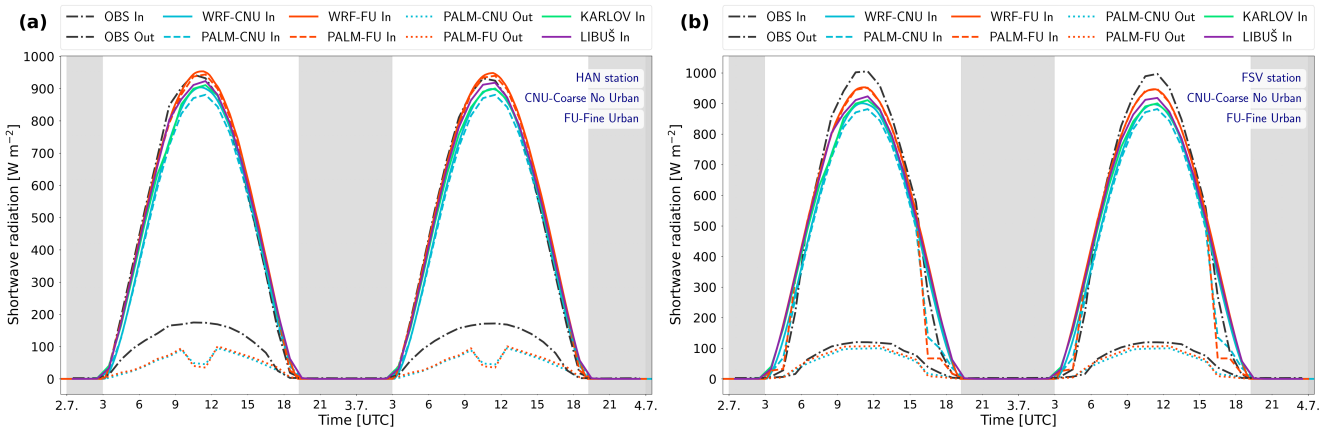

Figure 6. The comparison of observed hourly averages of incoming (In) and outgoing (Out) short-wave radiation for the e5 episode at the stations HAN (a) and FSV (b), with PALM model outputs for both WRF configurations. Additional lines represent the raw WRF outputs, Coarse No Urban (WRF-CNU), and Fine Urban (WRF-FU), and measurements from professional meteorological stations in Karlov and Libuš.

3.2.3 PALM's performance during non-clear sky conditions

As a physical factor, clouds are complex regulators of short-wave radiation flux, affecting both its magnitude and timing. Hence, the shape of the incoming short-wave radiation function during periods of variable cloud cover deviates from its clear-sky counterpart, which is roughly symmetrical with its maximum around solar noon. Caused by physical and numerical factors, the resolution and modelling of short-wave radiation under non-clear-sky conditions pose a challenge for all types of meteorological models, regardless of spatial resolution. In this section, we evaluate PALM's robustness in capturing radiation during non-idealised (i.e, non-clear-sky) cases through three selected episodes (e9, e10, and e12) characterised by cloudy or partly cloudy conditions (see Fig. 7). In the first analysed episode, e9, the advantages of PALM's downscaling are most evident at the vegetated FLE station (see Fig. 7a). Up to around midday, PALM diverges from its driving data and adjusts the SWin profile toward the observed values. However, after noon, PALM no longer matches the observations and aligns more closely with its driving data. The SWout shows a more uniform pattern, with PALM aligning well with the observed outgoing radiation in the morning hours, underestimating it around noon, and slightly overestimating it in the afternoon. For the same episode and the urban NTK station, both SWin and SWout discrepancies are large. PALM does not align with the observed values and follows its driving data entirely. These deviations at the NTK station are clearly seen through the quantitative evaluations presented in Table 5 and Table 6, as well as in the MBE and RMSE errors in Fig. 2. For episodes e10 and e11 at the FSV station, during the early morning hours (i.e., 3–6 am), PALM corrects its driving data and aligns the SWin profile with the observations. However, during midday in episode e10 and in the afternoon of episode e12, where the effect of the clouds is pronounced the most (Fig. 7b,c,e,f), PALM's downscaling cannot mitigate the incorrect information in the WRF data, which does not capture the clouds present at the Karlov and Libuš reference stations and at the observation sites. The identified

underestimation of SWout at the HAN station also persists during the non-clear-sky conditions, as seen in Fig. 7b,c. Both CNU and FU configurations exhibit bell-shaped SWin evolution, but the FU shows significantly higher values during the noon peak, while the CNU remains well below the observed values.

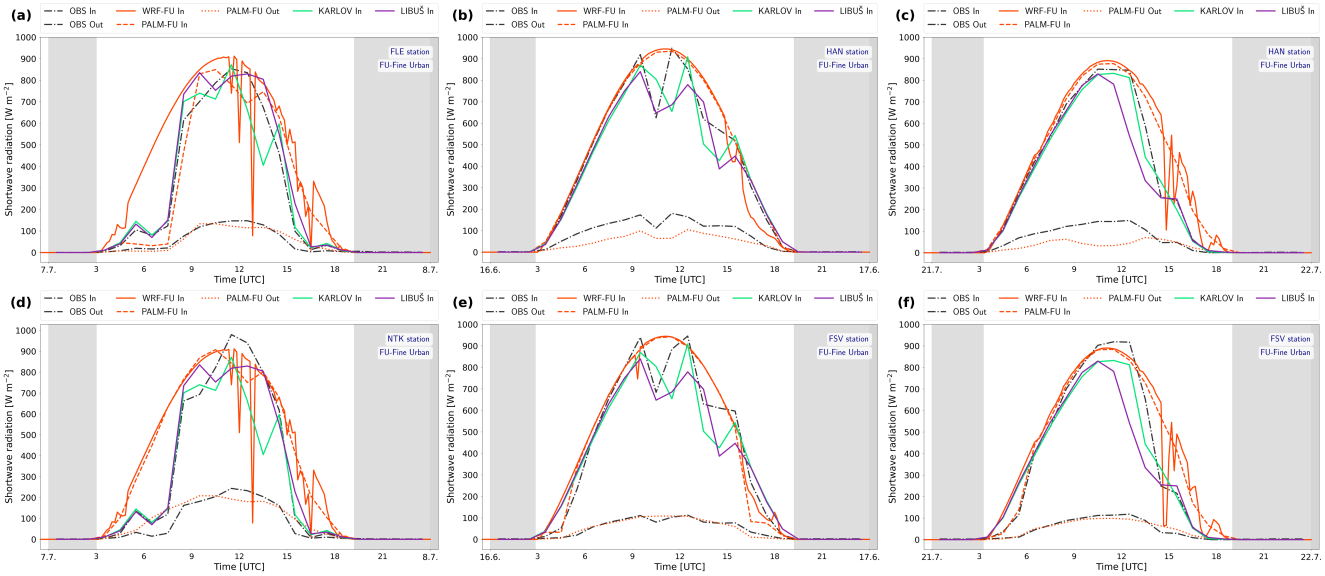

Figure 7. The comparison of observed hourly averages of incoming (In) and outgoing (Out) short-wave radiation during the non-clear sky episodes e9 (a.d), e10 (b,e), and e12 (c,f) at the selected station combinations, with PALM model outputs for both WRF configurations. Additional lines represent the raw WRF outputs, Coarse No Urban (WRF-CNU), and Fine Urban (WRF-FU), and measurements from professional meteorological stations in Karlov and Libuš.

4 Discussion

4.1 General model performance in simulating short-wave radiation

– **Shadow patterns of urban morphology in modelling incoming short-wave radiation.**

One of the key assets of PALM, identified in the study, is its ability to realistically simulate the magnitude of incoming short-wave radiation at morning and afternoon times as observed from street-level stations. Buildings, trees, and other obstacles cast the longest and broadest shadows during the hours when the Sun is near the horizon (i.e., early morning and late afternoon). Correctly reproducing the impact of urban obstructions (i.e., shadow patterns) on the detected SWin amount at the urban station requires explicitly integrating information on building and tree size, height, orientation, and spacing into the micro-scale model. At this point, the robustness of the RTM and PALM becomes evident: they can explicitly resolve sunlit and shaded surfaces and energy redistribution based on the calculated local sky view factors and shading geometry. Beyond their ability to resolve shading patterns, a further key aspect addressed by the micro-

scale model is the correct translation of this information into short-wave flux magnitudes at the 1 m scale. Moreover, the visible delay and attenuated magnitude of the PALM-simulated SWin are corrected relative to the WRF driving data, which most likely results from the WRF assuming unobstructed surfaces and therefore further overestimates SWin during these hours.

However, certain disagreements between the micro-scale outputs and the observation data, resulting from incorrect urban canopy representation in the micro-scale model, are also identified (see Fig. 8 FLE station around 15:00 UTC, for example, PALM's tree height is shorter than the real one, and SWin is not attenuated enough, and Fig. S12 NTK around 04:00 UTC, where the tree is not represented accurately in PALM as well). As said, incident short-wave radiation is highly sensitive to the placement and dimensions of urban obstacles, so even small inaccuracies in the PALM static driver data can produce excess attenuation or an increase in the incoming radiation in the PALM's outputs.

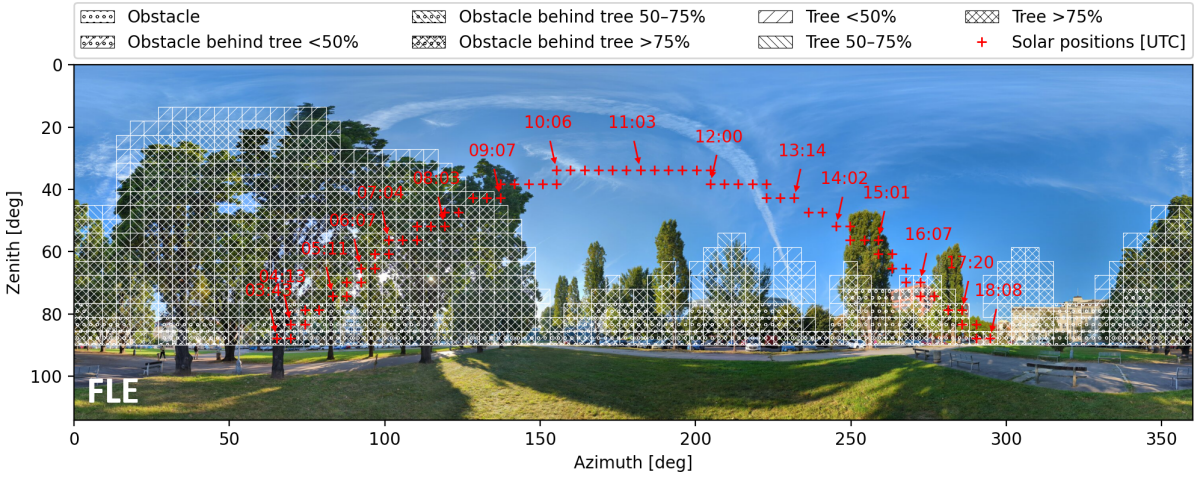

Figure 8. Hemispherical view at the FLE observation site with obstructions and vegetation as modelled by PALM, plotted in azimuth–zenith coordinates. Trees and obstacles are classified according to their fractional area coverage. Red crosses indicate the Sun's trajectory throughout the day, with annotated timestamps in UTC.

– **PALM's simulation of outgoing short-wave radiation.**

While the PALM model can simulate incoming short-wave radiation with a high degree of reliability at the 1 m scale, the outgoing short-wave radiation outputs indicate that modelling this variable poses a greater challenge for PALM and requires a more precise description of urban surface properties. The incoming short-wave radiation modelling is generally less challenging, as it is primarily governed by atmospheric transmissivity (e.g., cloud and aerosol presence) and the Sun's position in the sky. In contrast, outgoing short-wave radiation is heavily influenced by the three-dimensional urban form, surface albedo, complex multiple reflections within urban canyons, and the structure of the vegetation canopy.

The general settings of surface albedo for vegetation in the static driver proved to be a significant source of bias in PALM's modelling of reflected radiation. A good illustration supporting this statement is the HAN station, whose sur-

roundings are rich in vegetation and covered by grassland. As seen from the daily SWout profiles in Fig. 6, there is a significant reduction in the PALM modelled SWout during the midday hours. Such a drop in the SWout indicates low reflection at this location, and consequently strong absorption, implying that PALM represents this area with low-to-moderate albedo values (indeed, the prescribed albedo for HAN in PALM is 0.17). It appears that the PALM is unable to capture variability in grassy surfaces; the only option is a manual setup for individual episodes. In reality, the grass moving at this location was not, most likely, periodic, as the measured SWout signal indicates more reflection and weaker absorption. The reflection could also be affected by available soil moisture, which varies daily and seasonally and is typically not accurately captured by WRF. The negative bias at the HAN station could not be mitigated, even with the improved WRF-FU setup, since the underestimation of the SWout at HAN stayed significant (e.g., see Fig. 4). To further investigate the discrepancy in reflected short-wave radiation at the HAN station, one additional analysis was performed. Observed, and PALM modelled albedo at the FSV ("well-behaving") station and the problematic HAN station were compared for episode e5 (see Fig. S17). Albedo was calculated as the ratio between reflected and incoming short-wave radiation, and only periods with SWin $> 10\mathrm{Wm}^{-2}$ were considered. The observations indicate differences between the two observation stations. The HAN station exhibits substantially higher albedo than FSV throughout most of the daytime period. On the other hand, the PALM model reproduces the magnitude and temporal evolution of albedo at FSV reasonably well, while it underestimates albedo at the HAN station. The systematic low bias at HAN may indicate deficiencies in the representation of surface properties and land-cover characteristics that control surface albedo during the episode.

A notable tendency of the PALM model is a systematic underestimation of SWout, suggesting an excessive sink of short-wave radiation (i.e., pronounced negative MBE values, see Fig. 2a–c). These negative biases are attributable to the inaccurately represented vegetation, prescribed albedo, and geometric factors, rather than to biases in the meso-scale driving data or in the WRF model setup. This behaviour does not inherently imply poor performance of the micro-scale model; instead, it reflects the challenge of accurately simulating outgoing short-wave radiation in highly heterogeneous, densely built urban environments. Although the SWout magnitude is generally underestimated, PALM simulates its temporal evolution and variability very well, as evidenced by strong overall correlations (see Tab. 6). Furthermore, the scale of the MBE at the FSV, NTK, and FLE stations is generally smaller (despite the remaining underestimation), directly demonstrating PALM's capability to accurately assess reflections from complex urban geometry, canyon shading effects, and to provide sufficiently precise albedo values and urban surface properties.

– **Underprediction of the incident short-wave radiation at solar noon:** The systematic SWin underestimation at the evaluated stations around solar noon during the clear-sky episodes (mainly in the WRF-CNU setup) results from a "chain reaction" originating from the WRF's driving data supplied to PALM. PALM's modelling independence during this period is clearly limited, as it either amplifies or maintains the same level of bias in its outputs without imposing significant corrections, and it does not reach the peak intensity measured at the observation site. In principle, during clear-sky conditions at solar noon, the systematic underestimation of SWin is unlikely to be solely attributable to shadings induced by urban structures. At this time of day, the Sun's zenith angle is low, and the incoming short-wave radiation

travels nearly vertically. It minimises any geometry-induced shading or surface-based effects, suggesting that the SWin underestimation is most likely driven by other factors (e.g., the SWin definition before reaching the canopy height and the observation point within the micro-scale model domain).

The distinction between both WRF configurations' solar-noon performance reinforces the above argument; the WRF-FU configuration significantly reduces the solar-noon discrepancies that are clearly observed in the WRF-CNU runs (see e.g., Supplement Fig. S2). This suggests that the short-wave radiation inherited from the WRF-CNU driving data is the primary source of PALM's systematic noon bias. The PALM internal factors (e.g., RTM, USM, PCM, static driver data) play only a secondary role or may have no effect. Within the WRF model framework, several factors can lead to excessive underestimation. First, inaccuracies in WRF's driving data (i.e., ERA5) may introduce an overestimated amount of aerosols or water vapour concentrations in WRF simulations and bias its radiative calculations. Second, WRF's radiation scheme can itself overestimate the absorption and scattering by aerosols, water vapour or other atmospheric constituents within the WRF domain, and consequently overestimate the absorption and scattering of the actual amount of short-wave radiation. Alternatively, physical parameterisation in WRF's PBL schemes could lead to weak vertical mixing and trap moisture in the lower layers, further attenuating the magnitude of short-wave radiation. The PALM model inherits the bias and starts its simulations with reduced top-of-domain downwelling short-wave radiation. Since the SWin PALM's output magnitude is reduced relative to observations (and, in certain cases, even lower than its WRF driving data), the loss of the SWin magnitude between the top of PALM's domain and the sensor grid point could be caused by incorrectly modelled surface-sky radiative interactions. Potential error could lie in incorrect redistribution or underestimation of diffuse short-wave radiation within PALM's surface, canopy, and geometry-related routines. However, although PALM's internal modules can affect SWin underestimation, their influence is secondary to that of WRF.

4.2 Driving data impact: WRF-CNU vs. WRF-FU configuration performance

A primary outcome of the driving-data impact evaluation on micro-scale simulations is the added value of the FU and the lower accuracy of the CNU configuration for PALM micro-scale simulations. Although both setups reproduced temporal SWin evolution well relative to the observed values (with FU being more accurate), differences between them are reflected in the magnitude of bias and in overall statistical metrics of the evaluated PALM outputs.

The central differences between the two WRF setups are in their horizontal resolutions and physics parameterisation bundles as presented in Table 1. The CNU configuration does not include information on urban canopy, geometry, or three-dimensional objects (i.e., buildings) and has a coarser 3 km resolution. A combination of these WRF-CNU features produces smoother radiation fields and overestimates morning and late-afternoon incoming SW radiation by failing to account for urban physical structures and shadowing effects. The inability to represent building-involved shadowing effects is evident in the qualitative analysis, e.g., Fig. 5, where the WRF-CNU setup predicts an earlier and accelerated morning increase, as well as a delayed afternoon reduction in SW incoming radiation compared to the observation.

Another prominent distinction visible in Fig. 5a is that the PALM-CNU In to WRF-CNU In ratio differs substantially from the PALM-FU In to WRF-FU In ratio. The differences in the PALM-to-WRF short-wave radiation ratios at the FLE station

during the evaluated episode are closely related to differences between the diffuse (see Fig. S15) and direct short-wave radiation components (see Fig. S16). Namely, the WRF-CNU simulations exhibited substantially larger diffuse short-wave radiation (larger PALM/WRF ratio) than the WRF-FU simulations (smaller PALM/WRF ratio). These results, therefore, highlight that accurate representation of the diffuse and direct shortwave radiation components is crucial for reproducing total radiation fluxes, and that PALM simulations are sensitive to the diffuse/direct partitioning inherited from the mesoscale forcing model.

The improved resolution and more explicit treatment of urban morphology in the FU configuration benefit the FU-driven PALM simulation outputs. This is evidenced by improved overall statistical metrics (i.e., reduced MBE and RMSE and higher agreement metrics) and a lower difference between peak solar noon insolation and observations. Even though the WRF-FU setup's departure from observation in SWin is evident in morning and afternoon street-level shadowing patterns, its midday maxima are more realistic, and this configuration demonstrates a higher degree of agreement with observations from both CHMU and dedicated measurement stations. Finally, the FU's overall superiority is seen in reduced dispersion of PALM's SWin and SWout values (see Fig. 3 and Fig. 4).

Given these findings, the WRF-CNU driving dataset impairs PALM's performance due to biased radiation input fields, whereas the WRF-FU setup provides PALM with more accurate radiation fields. As previously demonstrated in Radović et al. (2024) and Resler et al. (2024) for meteorological variables (i.e., temperature and wind speed), this study emphasises both the importance of highly accurate radiation input fields and PALM's sensitivity to the quality of meso-scale radiation forcing. Since PALM's and the RTM's limited capability to simulate complex radiative transfer processes is insufficient to correct biases in the driving fields, supplying the micro-scale model with realistic and robust meso-scale radiation forcing is imperative.

4.3 The effects of sky conditions on micro-scale simulations

Undoubtedly, this study demonstrates clear performance degradation of the micro-scale model under non-clear-sky conditions relative to the clear-sky conditions, where PALM's RTM exhibits high-quality performance. During clear-sky conditions, the Sun's position relative to the Earth and the city's structure predominantly control the radiation field. In such cases, PALM's RTM modelling, with meter-scale resolution, explicitly resolves the detailed processes that affect radiation fluxes and accurately simulates the spatio-temporal dynamics of incoming short-wave radiation (i.e., exhibiting high temporal coherence with observations, good magnitude and phase alignment, and strong statistical performance). When the variability in incoming radiative fluxes is caused by intermittent cloud cover, PALM's framework is unable to capture rapid spatiotemporal fluctuations in radiative fluxes because it depends on information from the meso-scale model. The performance degradation is more pronounced in PALM's SWin outputs, as evidenced by overestimated incoming radiation, low correlation, and generally poor statistical performance. PALM's ability to accurately capture and redistribute radiation based on finely detailed, high-resolution geometry is insufficient for capturing the effects of cloud pattern shifts. Under cloud-cover conditions, the PALM is driven by the input conditions given by WRF. Temporal mismatches in cloud passages lead to large discrepancies in radiation values, thereby further reducing correlation and increasing relative errors. However, it is important to keep in mind that PALM's limited fidelity under non-clear-sky conditions does not represent a failure of the model itself and that its predictive skill remains reasonably good.

4.4 The importance of accurate short-wave radiation modelling for urban climate research and climate change adaptation and mitigation

Short-wave radiative fluxes play a critical role in urban surface energy balance and strongly control urban climate, thermal comfort, and energy consumption in urbanised areas. If they are not captured accurately, errors and uncertainties in the radiative fluxes computed by PALM's RTM will propagate through the rest of the model framework and, in turn, affect all other variables that depend on them, thereby diminishing the overall reliability of the simulation. Establishing reliable simulations is especially important when the micro-scale model is applied to human biometeorological studies or to the development of urban adaptation or mitigation scenarios.

In human biometeorology, particularly in cities, SWin and SWout are crucial for estimating the thermal exposure and evaluating human thermal comfort. In essence, these two variables govern the MRT, the most important variable for calculating thermal comfort indices such as UTCI and PET. The incoming short-wave radiation determines the level of solar exposure within cities (e.g., in sunlit areas such as open squares, wide streets, large public squares and plazas, and similar spaces). In contrast, reflected short-wave radiation contributes to the amount of radiative load imposed by buildings, roads, and surrounding surfaces on urban dwellers. Inaccurate calculations of these radiative variables can lead to misidentification and mapping of heat-vulnerable locations within cities, as well as to incorrect assessments of both the magnitude and the spatial distribution of heat stress.

From an application perspective, precise short-wave flux calculations are crucial for urban planning and design purposes, as well as for the development of mitigation strategies. Since the amount of SWin cannot be controlled, its precise and high-resolution modelling is fundamental to urban planning and design; without it, the strategic arrangement and optimisation of building orientation and placement, street layouts, shade sail installation, and tree positioning would be less effective. In certain situations, inappropriate mitigations may fail, leading to increased heat stress, distorted heating and cooling loads, and reduced overall urban sustainability. On the other hand, the SWout is a variable that urban planners can "control" to a certain extent, as it can be altered by choosing urban materials that, for example, promote cooling. Our results emphasise the high sensitivity of the SWout to the input static driver data. Hence, effectively simulating any pavement-based mitigation strategy or evaluating pavement albedos requires both reliable urban static driver datasets and fidelity in PALM's SWout calculation procedures. Only if these two conditions are met can the predicted benefits and drawbacks of a designed strategy be considered realistic and applicable to urban sustainability planning (e.g., urban heat mitigation, thermal comfort improvements, and the long-term resilience of cities).

4.5 Limitations and future aspects

– **Static driver data accuracy constraints:** Despite substantial efforts to ensure data quality (see section 3.2 in Resler et al., 2021), PALM's static driver dataset is inherently prone to inaccuracies in urban morphology, land cover, and vegetation characteristics. This makes it a weak link in the micro-scale simulation framework and a major source of internally driven uncertainty, because it is practically impossible to map and keep all urban surfaces up to date. Due to

the high heterogeneity of urban elements within the micro-scale simulation domain, uncertainties can arise from any component defined in the static dataset (Belda et al., 2021). They can lead to systematic errors that directly affect both SWin and SWout. Static driver data that may be erroneous includes, for example, building height and location, roof geometry, surface material, surface optical properties (e.g., albedo), vegetation height and spatial placement, and leaf area density. Spherical photography at the measurement location can be used to identify these discrepancies as potential sources of errors, as shown in Figure 8.

Simplified or idealised albedos and their deviations from actual "real-world" values for roofs, walls, pavements, and vegetated surfaces are the main contributors to incorrect estimates of reflected radiation (as illustrated at the HAN station). In addition, these incorrectly represented albedos also affect the final value of the modelled SWin, owing to the multiple-reflection processes represented and permitted by PALM's RTM. In reality, urban objects, surfaces and vegetation are not "static" – they are prone to change due to ageing, season, and temporary or permanent human modification. Since such limitations inevitably reduce simulation accuracy, future work should prioritise continuous updates to urban morphology datasets and their utilisation in micro-scale models, such as PALM.

- **Limitations imposed by the meso-scale driving data:** PALM's modelling freedom is limited by its dependence on the meso-scale driving data, as demonstrated throughout this work. The meso-scale errors propagate to micro-scale simulations, introducing significant biases in PALM's radiation-dependent variables and outputs. Therefore, future studies should focus on improving the accuracy of cloud development, transfer, and optical properties within the meso-scale model, and on assessing its reliability prior to conducting simulations. This would significantly strengthen confidence in PALM's applicability under non-clear-sky conditions and further enhance the fidelity of its simulations, even when it already performs well under clear-sky conditions. From an objective standpoint, future studies should focus on developing and refining more sophisticated coupling strategies for meso-scale and micro-scale models.

- **Observational limitations:** Our validation is not supported by a dense observation network but is performed against four point-based measurement locations that cover only a limited spatial area. Consequently, this study is inherently constrained by a limited spatial sampling and may not fully reflect PALM's fidelity in capturing radiation variability within the simulated domain. Future efforts should prioritise establishing a denser and more heterogeneous observational network to enable a more comprehensive evaluation of the micro-scale model.

- **Transferability and representativeness of the results:** This analysis presents a case study of a unique urban configuration in Prague that encompasses both densely built-up areas and vegetation-covered environments. Hence, the validation and performance evaluation of PALM's RTM remain specific to this context; applying the modelling framework to a different city or urban environment may reveal limitations not captured within the simulation domain used in this study. Furthermore, this study assesses only a limited number of episodes during the summers of 2017 and 2018. Conclusions drawn from this ensemble of episodes may not be transferable to other seasons, even though these episodes were deliberately selected for their relevance to, e.g., urban heat stress.

5 Conclusions

The central objective of this study is to examine the ability of the micro-scale model PALM to simulate both incoming and outgoing short-wave radiation in a densely built urban environment. Following that, the experiment investigates how structurally complex urban morphology and vegetation modulate these radiative fluxes and exposes the uncertainties arising from meso-scale driving conditions and their effects on the micro-scale simulation. This was achieved by validating the micro-scale simulations against observed incoming and reflected radiation at four locations, each with different urban morphological properties, under various atmospheric cloud coverages. The PALM simulations are driven by two differently configured sets of boundary conditions from the meso-scale model WRF. Next, both qualitative and quantitative analyses of PALM-modelled radiative exchanges between buildings, pavements, and vegetation, as well as an evaluation of the uncertainties introduced by the driving data, are performed. In conclusion, the performed experiment has led to the following findings:

- The validation results showed the high fidelity of the micro-scale model in resolving the spatial and temporal variability of short-wave radiation in a radiatively complex, morphologically heterogeneous urban environment. The model is particularly robust in accounting for shading effects from buildings, treating multiple reflections within urban canyons, and vegetation-induced attenuation of short-wave radiation.

- From the PALM simulations, it is particularly noticeable how morphology and vegetation strongly influence the distribution of short-wave radiation at the one-meter scale. From a micro-scale modelling perspective, accurate reproduction of morning and evening shading patterns validates both the model's physical consistency in representing urban radiative processes and the correct implementation of the urban static driver dataset within the model's framework. On the other hand, this alteration of both incoming and reflected radiation is not resolved in coarser models like WRF. Hence, because PALM realistically reflects the spatial and morphological heterogeneity of the urban environment and improves the representation and calculation of urban radiative processes, it can be considered a reliable tool for urban climate assessment.

- The reliability of the high-resolution micro-scale model simulations is especially dependent on the quality of the driving data and the prescribed urban static driver dataset. Moreover, as an important outcome, we highlight that realistically represented downwelling radiation from the meso-scale model and the boundary conditions are indispensable for obtaining reliable results from PALM's high-resolution modelling framework. If the imposed meso-scale driving data does not reflect actual radiative and meteorological weather conditions and contains errors, the micro-scale model will inherit these inaccuracies, thereby constraining the reliability of its simulations. To manage this complex and significant issue, both meso-scale downwelling radiation and boundary conditions must be rigorously verified. Without prior examination of the driving data and the attribution of potential discrepancies, any interpretation of the micro-scale outputs remains restricted and unreliable.

- Building on the previous argument, the simulated cloud cover in the meso-scale model stands out as the most important physical driver and an essential source of potential uncertainty, because even the small inaccuracies in their representation

can produce large deviations in downwelling short-wave radiation supplied to the micro-scale model. Therefore, future research should focus on improving the accuracy of cloud representation and cloud-related parameters in the driving data. This could be achieved using ceilometer measurements, all-sky imaging systems, satellite-derived cloud datasets, or machine-learning-based cloud reconstruction methods. Fine-tuned cloud depiction would substantially improve the coherence between real atmospheric conditions and meso-scale forcings, as well as between the meso-scale forcings and micro-scale simulations. Consequently, existing and potential biases could be removed from the meso-scale forcing, preventing further error propagation into the micro-scale simulation.

As a micro-scale model, PALM accounts for the propagation and interaction of short-wave radiation within a city's complex geometry; however, the consistency and quality of its output ultimately depend on the quality and accuracy of the prescribed static datasets and the meso-scale input forcing data. Finally, the experiment underscores that achieving PALM's high-level predictive skill and generating reliable, climate-sensitive urban resilience strategies require prior examination of the driving datasets, along with methodical diagnostics and quantification of their underlying biases.

Code and data availability. The utilised source code, the PALM installation and usage guide description, the PALM model input data, the WRF model configuration files, and the observational datasets used for validation are stored at: https://doi.org/10.5281/zenodo.19231961 (Radović et al., 2026).

Author contributions. J. Radović: Conceptualisation, Data curation, Formal analysis, Investigation, Methodology, Software, Supervision, Validation, Visualisation, Writing – original draft, Writing - Review & Editing. M. Belda: Formal analysis, Investigation, Writing - Review & Editing. M. Bureš: Data curation, Software, Validation, Visualisation. K. Eben: Software, Validation. Writing – review & editing. J. Geletič: Conceptualisation, Data curation, Formal analysis, Investigation, Methodology, Software, Supervision, Validation, Visualisation, Writing – original draft, Writing – review & editing. J. Jura: Data curation. P. Krč: Funding acquisition, Project administration, Data curation, Formal analysis, Software, Validation, Visualisation, Writing – review & editing. H. Řezníček: Writing – review & editing. J. Resler: Conceptualisation, Funding acquisition, Project administration, Supervision, Software, Validation, Writing – review and editing.

Competing interests. The authors declare that they have no conflict of interest.

Acknowledgements. This work was supported by the Johannes Amos Comenius Programme (P JAC) project Natural and anthropogenic georisks (No. CZ.02.01.01/00/22_008/0004605), by the MICROBUS project, which is financed from the state budget by the Technology Agency of the Czech Republic and the Ministry of the Environment within the "Prostředí pro život 2" Programme, by the project Strategy AV21 Dynamic Planet Earth. The PALM simulations were performed on the HPC infrastructure of the IT4I supercomputing center supported by the Ministry of Education, Youth and Sports of the Czech Republic through the e-INFRA CZ (ID no. 90254). The WRF simulations, as

well as pre- and postprocessing, were conducted on the HPC infrastructure of the Institute of Computer Science (ICS) of the Czech Academy of Sciences supported by the long-term strategic development financing of the ICS (RVO 67985807). The authors utilised Grammarly for grammatical verification and to refine the scientific text throughout the drafting process.

Appendix A: Statistical evaluation

Considering that M_i is the PALM-simulated value, $\overline{M}$ is the mean of all PALM-simulated values, O_i is the observed value, $\overline{O}$ is the mean of the observations, and n is the total number of paired samples, the following formulas are applied for the statistical evaluation:

1. **Mean Bias Error MBE** $\mathrm{MBE} = \frac{1}{n}\sum_{i=1}^{n}(M_i - O_i)$
2. **Root Mean Square Error RMSE** $\mathrm{RMSE} = \sqrt{\frac{1}{n}\sum_{i=1}^{n}(M_i - O_i)^2}$
3. **Pearson correlation coefficient r**

$$\mathrm{r} = \frac{\sum_{i=1}^{n}(M_i - \overline{M})(O_i - \overline{O})}{\sqrt{\sum_{i=1}^{n}(M_i - \overline{M})^2 - \sum_{i=1}^{n}(O_i - \overline{O})^2}}$$

4. **Coefficient of determination** R^2

$$\mathrm{R}^2 = 1 - \frac{\sum_{i=1}^{n}(O_i - M_i)^2}{\sum_{i=1}^{n}(O_i - \overline{O})^2}$$

5. **Spearman's correlation coefficient** ρ

$$\rho = 1 - \frac{6\sum_{i=1}^{n} d_i^2}{\cdot} n(n^2-1); d_i = \mathrm{rank}(M_i) - \mathrm{rank}(O_i)$$

6. **Kendall's correlation coefficient** τ

$$\tau = \frac{N_c - N_d}{\frac{1}{2}n(n^2-1)}; \text{where } N_c \text{ and } N_d \text{ are the numbers of concordant and discordant pairs, respectively.}$$

7. **Index of Agreement (d; Willmott, 1981)**

$$d = 1 - \frac{\sum_{i=1}^{n}(M_i - O_i)^2}{\sum_{i=1}^{n}(|M_i - \overline{O}| + |O_i - \overline{O}|)^2}$$

8. **Absolute difference AD**

$$\mathrm{AD} = \frac{1}{n}\sum_{i=1}^{n}|M_i - O_i|$$

9. **Relative Difference RD**

$$\mathrm{RD} = \frac{1}{n}\sum_{i=1}^{n}\left(\frac{M_i - O_i}{O_i}\right) \times 100\%$$

Appendix B: WRF-to-PALM modelling workflow

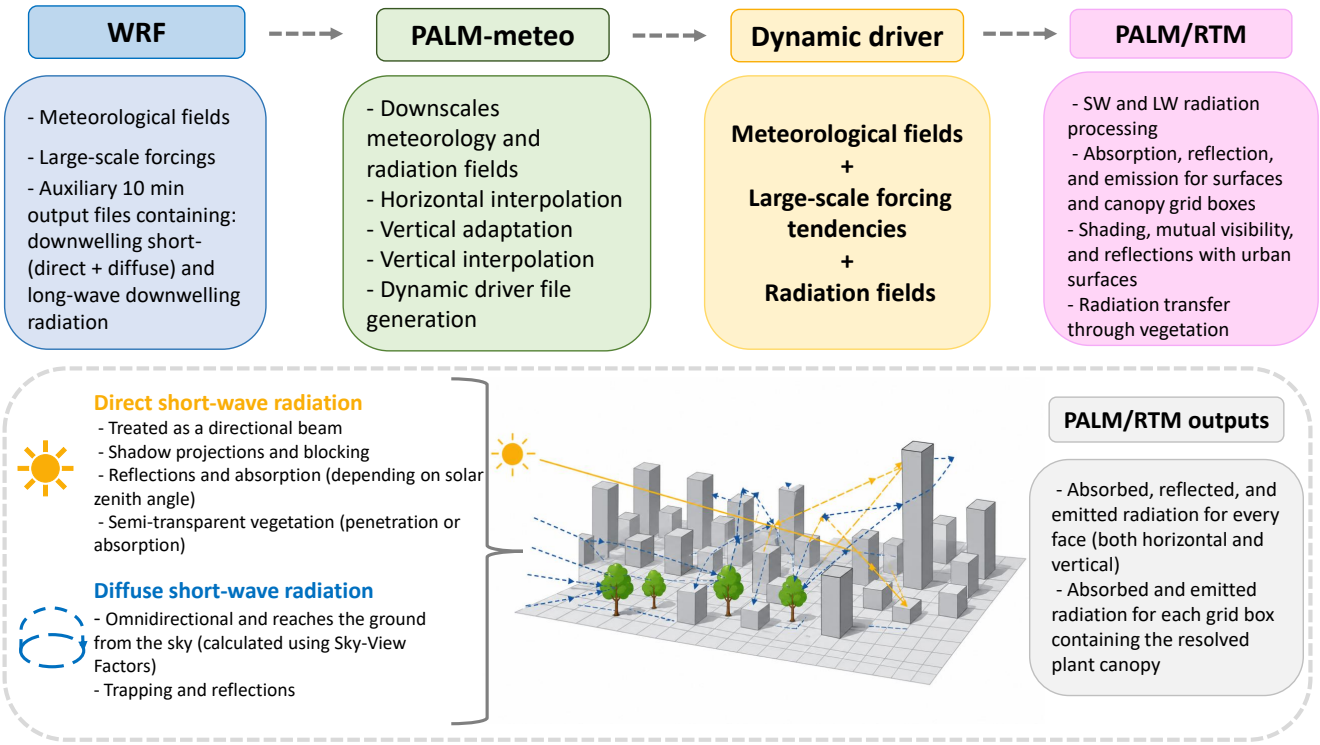

Figure B1. Schematic representation of the WRF-to-PALM modelling workflow applied in this study. The figure illustrates how meteorological and radiation fields are passed from the WRF model through the PALM-meteo processor and the dynamic driver file into PALM and its radiation transfer module (RTM).

References

Aminipouri, M., Knudby, A. J., Krayenhoff, E. S., Zickfeld, K., and Middel, A.: Modelling the impact of increased street tree cover on mean radiant temperature across Vancouver's local climate zones, Urban Forestry & Urban Greening, 39, 9–17, https://doi.org/10.1016/j.ufug.2019.01.016, 2019.

Aoyagi, T. and Takahashi, S.: Development of an Urban Multilayer Radiation Scheme and Its Application to the Urban Surface Warming Potential, Boundary-Layer Meteorology, 142, 305–328, https://doi.org/10.1007/s10546-011-9679-0, 2012.

Baklanov, A., Grimmond, C. S. B., Carlson, D., Terblanche, D., Tang, X., Bouchet, V., Lee, B., Langendijk, G., Kolli, R. K., and Hovsepyan, A.: From urban meteorology, climate and environment research to integrated city services, Urban Climate, 23, 330–341, https://doi.org/10.1016/j.uclim.2017.05.004, 2018.

Belda, M., Resler, J., Geletič, J., Krč, P., Maronga, B., Sühring, M., Kurppa, M., Kanani-Sühring, F., Fuka, V., Eben, K., et al.: Sensitivity analysis of the PALM model system 6.0 in the urban environment, Geoscientific Model Development, 14, 4443–4464, https://doi.org/10.5194/gmd-14-4443-2021, 2021.

Blocken, B.: Computational Fluid Dynamics for urban physics: Importance, scales, possibilities, limitations and ten tips and tricks towards accurate and reliable simulations, Building and Environment, 91, 219–245, https://doi.org/10.1016/j.buildenv.2015.02.015, 2015.

Blocken, B.: LES over RANS in building simulation for outdoor and indoor applications: A foregone conclusion?, Building Simulation, 11, 821–870, https://doi.org/10.1007/s12273-018-0459-3, 2018.

Bougeault, P. and Lacarrere, P.: Parameterization of Orography-Induced Turbulence in a Mesobeta–Scale Model, Monthly Weather Review, 117, 1872 – 1890, https://doi.org/10.1175/1520-0493(1989)117<1872:POOITI>2.0.CO;2, 1989.

Bruse, M., Simon, H., and Sinsel, T.: Development and implementation of a high-resolution dynamical wall and roof model for ENVI-met. Part 1: General model design and non-vegetated walls and roofs, https://doi.org/10.13140/RG.2.2.29309.95207, [cited 8.10.2025], 2023a.

Bruse, M., Simon, H., and Sinsel, T.: Development and implementation of a high-resolution dynamical wall and roof model for ENVI-met. Part 2: Vegetated walls and roofs, https://doi.org/10.13140/RG.2.2.36020.83842, [cited 8.10.2025], 2023b.

Chen, L., Yu, B., Yang, F., and Mayer, H.: Intra-urban differences of mean radiant temperature in different urban settings in Shanghai and implications for heat stress under heat waves: A GIS-based approach, Energy and Buildings, 130, 829–842, https://doi.org/10.1016/j.enbuild.2016.09.014, 2016.

Chen, T., Pan, H., Lu, M., Hang, J., Lam, C. K. C., Yuan, C., and Pearlmutter, D.: Effects of tree plantings and aspect ratios on pedestrian visual and thermal comfort using scaled outdoor experiments, Science of the Total Environment, 801, 149 527, https://doi.org/10.1016/j.scitotenv.2021.149527, 2021.

Clough, S., Shephard, M., Mlawer, E., Delamere, J., Iacono, M., Cady-Pereira, K., Boukabara, S., and Brown, P.: Atmospheric radiative transfer modeling: a summary of the AER codes, Journal of Quantitative Spectroscopy and Radiative Transfer, 91, 233–244, https://doi.org/10.1016/j.jqsrt.2004.05.058, 2005.

Dirksen, M., Ronda, R., Theeuwes, N., and Pagani, G.: Sky view factor calculations and its application in urban heat island studies, Urban Climate, 30, 100 498, https://doi.org/10.1016/j.uclim.2019.100498, 2019.

Dudhia, J.: Numerical study of convection observed during the winter monsoon experiment using a mesoscale two-dimensional model, Journal of the Atmospheric Sciences, 46, 3077–3107, https://doi.org/10.1016/j.uclim.2019.100498, 1989.

Fanger, P. O.: Calculation of thermal comfort: Introduction of a basic comfort equation, ASHRAE Transactions, 73, III4.1–III4.20, 1967.

Freitas, S., Catita, C., Redweik, P., and Brito, M. C.: Modelling solar potential in the urban environment: State-of-the-art review, Renewable and Sustainable Energy Reviews, 41, 915–931, https://doi.org/10.1016/j.rser.2014.08.060, 2015.

Fröhlich, D. and Matzarakis, A.: Spatial Estimation of Thermal Indices in Urban Areas—Basics of the SkyHelios Model, Atmosphere, 9, 209, https://doi.org/10.3390/atmos9060209, 2018.

Fröhlich, D., Gangwisch, M., and Matzarakis, A.: Effect of radiation and wind on thermal comfort in urban environments - Application of the RayMan and SkyHelios model, Urban Climate, 27, 1–7, https://doi.org/10.1016/j.uclim.2018.10.006, 2019.

Gehrke, K. F., Sühring, M., and Maronga, B.: Modeling of land–surface interactions in the PALM model system 6.0: land surface model description, first evaluation, and sensitivity to model parameters, Geoscientific Model Development, 14, 5307–5329, https://doi.org/10.5194/gmd-14-5307-2021, 2021.

Geletič, J., Lehnert, M., Resler, J., Krč, P., Middel, A., Krayenhoff, E., and Krüger, E.: High-fidelity simulation of the effects of street trees, green roofs and green walls on the distribution of thermal exposure in Prague-Dejvice, Building and Environment, 223, 109 484, https://doi.org/10.1016/j.buildenv.2022.109484, 2022.

Geletič, J., Lehnert, M., Resler, J., Krč, P., Bureš, M., Urban, A., and Krayenhoff, E.: Heat exposure variations and mitigation in a densely populated neighborhood during a hot day: Towards a people-oriented approach to urban climate management, Building and Environment, 242, 110 564, https://doi.org/10.1016/j.buildenv.2023.110564, 2023.

Geletič, J., Lehnert, M., Krč, P., Resler, J., and Krayenhoff, E.: High-Resolution Modelling of Thermal Exposure during a Hot Spell: A Case Study Using PALM-4U in Prague, Czech Republic, Atmosphere, 12, 175, https://doi.org/10.3390/atmos12020175, 2021.

Grylls, T. and van Reeuwijk, M.: How trees affect urban air quality: It depends on the source, Atmospheric Environment, 290, 119 275, https://doi.org/10.1016/j.atmosenv.2022.119275, 2022.

Gál, C. V. and Kántor, N.: Modeling mean radiant temperature in outdoor spaces, A comparative numerical simulation and validation study, Urban Climate, 32, 100 571, https://doi.org/10.1016/j.uclim.2019.100571, 2020.

Hersbach, H., Bell, B., Berrisford, P., Hirahara, S., Horányi, A., Muñoz-Sabater, J., Nicolas, J., Peubey, C., Radu, R., Schepers, D., Simmons, A., Soci, C., Abdalla, S., Abellan, X., Balsamo, G., Bechtold, P., Biavati, G., Bidlot, J., Bonavita, M., De Chiara, G., Dahlgren, P., Dee, D., Diamantakis, M., Dragani, R., Flemming, J., Forbes, R., Fuentes, M., Geer, A., Haimberger, L., Healy, S., Hogan, J. R., Hólm, E., Janisková, M., Keeley, S., Laloyaux, P., Lopez, P., Lupu, C., Radnoti, G., de Rosnay, P., Rozum, I., Vamborg, F., Villaume, S., and Thépaut, J.-N.: The ERA5 global reanalysis, Quarterly Journal of the Royal Meteorological Society, 146, 1999–2049, https://doi.org/https://doi.org/10.1002/qj.3803, 2020.

Hogan, R. J. and Bozzo, A.: A Flexible and Efficient Radiation Scheme for the ECMWF Model, Journal of Advances in Modeling Earth Systems, 10, 1990–2008, https://doi.org/https://doi.org/10.1029/2018MS001364, 2018.

Holtanová, E., Belda, M., Randriatsara, H., Szabó, A. I., and Halenka, T.: Scenarios of Köppen-Trewartha climate types in Europe based on GCM-RCM combined projections, Theoretical and Applied Climatology, 156, https://doi.org/10.1007/s00704-025-05806-3, 2025.

Höppe, P. R.: The physiological equivalent temperature – a universal index for the biometeorological assessment of the thermal environment, International Journal of Biometeorology, 43, 71–75, https://doi.org/10.1007/s004840050118, 1999.

Iacono, M. J., Delamere, J. S., Mlawer, E. J., Shephard, M. W., Clough, S. A., and Collins, W. D.: Radiative forcing by long-lived greenhouse gases: Calculations with the AER radiative transfer models, Journal of Geophysical Research: Atmospheres, 113, https://doi.org/https://doi.org/10.1029/2008JD009944, 2008.

Jakub, F. and Mayer, B.: 3-D radiative transfer in large-eddy simulations – experiences coupling the TenStream solver to the UCLA-LES, Geoscientific Model Development, 9, 1413–1422, https://doi.org/10.5194/gmd-9-1413-2016, 2016.

Jänicke, B., Meier, F., Hoelscher, M., and Scherer, D.: Evaluating the effects of façade greening on human bioclimate in a complex urban environment, Advances in Meteorology, 14, 747 259, https://doi.org/10.1155/2015/747259, 2015.

Jendritzky, G., de Dear, R., and Havenith, G.: UTCI – Why another thermal index?, International Journal of Biometeorology, 56, 421–428, https://doi.org/10.1007/s00484-011-0513-7, 2012.

Jimenez, P. A., Dudhia, J., Gonzalez–Rouco, J. F., Navarro, J., Montavez, J. P., and Garcia–Bustamante, E.: A revised scheme for the WRF surface layer formulation, Monthly Weather Review, 140, 898–918, https://doi.org/10.1175/MWR-D-11-00056.1, 2012.

Jura, J., Novák, M., Bíla, J., Pokorný, J., and Jirka, V.: Hydrometeorological measurements to assess the effect of vegetation on urban microclimate, in: 2018 Smart City Symposium Prague, pp. 1–5, https://doi.org/10.1109/SCSP.2018.8402653, 2018.

Kadasch, E., Sühring, M., Gronemeier, T., and Raasch, S.: Mesoscale nesting interface of the PALM model system 6.0, Geoscientific Model Development, 14, 5435–5465, https://doi.org/10.5194/gmd-14-5435-2021, 2021.

Kondo, J.: Meteorology of water environment: Water and heat budgets at ground surface, Asakura Press, Tokyo: Japan, 1994.

Krč, P., Resler, J., Sühring, M., Schubert, S., Salim, M. H., and Fuka, V.: Radiative Transfer Model 3.0 integrated into the PALM model system 6.0, Geoscientific Model Development, 14, 3095–3120, https://doi.org/10.5194/gmd-14-3095-2021, 2021.

Krč, P., Belda, M., Bureš, M., Eben, K., Geletič, J., Radović, J., Řezníček, H., and Resler, J.: PALM-meteo 2.6: Processor of PALM meteorological input data, EGUsphere, 2025, 1–32, https://doi.org/10.5194/egusphere-2025-4120, 2025.

Kubilay, A., Allegrini, J., Strebel, D., Zhao, Y., Derome, D., and Carmeliet, J.: Advancement in Urban Climate Modelling at Local Scale: Urban Heat Island Mitigation and Building Cooling Demand, Atmosphere, 11, https://doi.org/10.3390/atmos11121313, 2020.

Kusaka, H., Ikeda, R., Sato, T., Iizuka, S., and Boku, T.: Development of a Multi-Scale Meteorological Large-Eddy Simulation Model for Urban Thermal Environmental Studies: The "City-LES" Model Version 2.0, Journal of Advances in Modeling Earth Systems, 16, e2024MS004 367, https://doi.org/10.1029/2024MS004367, 2024.

Kántor, N., Gál, C., Gulyás, Á., and Unger, J.: The impact of façade orientation and woody vegetation on summertime heat stress patterns in a central European square: comparison of radiation measurements and simulations, Advances in Meteorology, p. 2650642, https://doi.org/10.5194/gmd-14-5435-2021, 2018.

Lee, H., Mayer, H., and Schindler, D.: Importance of 3-D radiant flux densities for outdoor human thermal comfort on clear-sky summer days in Freiburg, Southwest Germany, Meteorologische Zeitschrift, 23, 315–330, https://doi.org/10.1127/0941-2948/2014/0536, 2014.

Lehnert, M., Pánek, J., Kopp, J., Geletič, J., Květoňová, V., and Jurek, M.: Thermal comfort in urban areas on hot summer days and its improvement through participatory mapping: A case study of two Central European cities, Landscape and Urban Planning, 233, 104 713, https://doi.org/10.1016/j.landurbplan.2023.104713, 2023.

Lindberg, F., Holmer, B., and Thorsson, S.: SOLWEIG 1.0 – Modelling spatial variations of 3D radiant fluxes and mean radiant temperature in complex urban settings, International Journal of Biometeorology, 52, 697–713, https://doi.org/10.1007/s00484-008-0162-7, 2008.

Liu, D., Hu, S., and Liu, J.: Contrasting the performance capabilities of urban radiation field between three microclimate simulation tools, Building and Environment, 175, 106 789, https://doi.org/10.1016/j.buildenv.2020.106789, 2020.

Liu, Z., Zheng, S., and Zhao, L.: Evaluation of the ENVI-Met Vegetation Model of Four Common Tree Species in a Subtropical Hot-Humid Area, Atmosphere, 9, 198, https://doi.org/10.3390/atmos9050198, 2018.

Maronga, B., Gryschka, M., Heinze, R., Hoffmann, F., Kanani-Sühring, F., Keck, M., Ketelsen, K., Letzel, M. O., Sühring, M., and Raasch, S.: The Parallelized Large-Eddy Simulation Model (PALM) version 4.0 for atmospheric and oceanic flows: model formulation, recent developments, and future perspectives, Geoscientific Model Development, 8, 2515–2551, https://doi.org/10.5194/gmd-8-2515-2015, 2015.

Maronga, B., Banzhaf, S., Burmeister, C., Esch, T., Forkel, R., Fröhlich, D., Fuka, V., Gehrke, K. F., Geletič, J., Giersch, S., et al.: Overview of the PALM model system 6.0, Geoscientific Model Development, 13, 1335–1372, https://doi.org/10.5194/gmd-13-1335-2020, 2020.

Martilli, A., Clappier, A., and Rotach, M.: An Urban Surface Exchange Parameterisation for Mesoscale Models, Boundary-Layer Meteorology, p. 261–304, https://doi.org/https://doi.org/10.1023/A:1016099921195, 2002.

Matuschek, O. and Matzarakis, A.: A mapping tool for climatological applications, Meteorological Applications, 18, 230–237, https://doi.org/10.1002/met.233, 2011.

Matzarakis, A., Rutz, F., and Mayer, H.: Modelling radiation fluxes in simple and complex environments—Application of the RayMan model, International Journal of Biometeorology, 51, 323–334, https://doi.org/10.1007/s00484-006-0061-8, 2007.

Matzarakis, A., Rutz, F., and Mayer, H.: Modelling radiation fluxes in simple and complex environments: basics of the RayMan model, International Journal of Biometeorology, 54, 131–139, https://doi.org/10.1007/s00484-009-0261-0, 2010.

Middel, A., Lukasczyk, J., and Maciejewski, R.: Sky View Factors from Synthetic Fisheye Photos for Thermal Comfort Routing—A Case Study in Phoenix, Arizona, Urban Planning, 2, 19–30, https://doi.org/10.17645/up.v2i1.855, 2017.

Mlawer, E. J., Taubman, S. J., Brown, P. D., Iacono, M. J., and Clough, S. A.: Radiative transfer for inhomogeneous atmospheres: RRTM, a validated correlated-k model for the longwave, Journal of Geophysical Research, 102, 16 663–16 682, https://doi.org/10.1029/97JD00237, 1997.

Nakanishi, M. and Niino, H.: Development of an Improved Turbulence Closure Model for the Atmospheric Boundary Layer, Journal of the Meteorological Society of Japan. Ser. II, 87, 895–912, https://doi.org/10.2151/jmsj.87.895, 2009.

Oke, T. R., Mills, G., Christen, A., and Voogt, J. A.: Urban climates, Cambridge University Press, https://doi.org/10.1017/9781139016476, 2017.

Piselli, C., Castaldo, V., Pigliautile, I., Pisello, A., and Cotana, F.: Outdoor comfort conditions in urban areas: On citizens' perspective about microclimate mitigation of urban transit areas, Sustainable Cities and Society, 39, 16–36, https://doi.org/10.1016/j.scs.2018.02.004, 2018.

Radović, J., Belda, M., Resler, J., Eben, K., Bureš, M., Geletič, J., Krč, P., Řezníček, H., and Fuka, V.: Challenges of constructing and selecting the "perfect" boundary conditions for the large-eddy simulation model PALM, Geoscientific Model Development, 17, 2901–2927, https://doi.org/10.5194/gmd-17-2901-2024, 2024.

Radović, J., Belda, M., Bureš, M., Eben, K., Jan, G., Jura, J., Krč, P., Řezníček, H., and Resler, J.: Dataset: Evaluating the radiative fidelity of PALM (v25.04) in high-resolution: impact of diverse urban morphology and vegetation on short-wave radiation, https://doi.org/10.5281/zenodo.19231961, last access: March 2026, 2026.

Rao, V. R. and Sastri, V. M. K.: Efficient evaluation of diffuse view factors for radiation, International Journal of Heat and Mass Transfer, 39, 1281–1286, https://doi.org/10.1016/0017-9310(95)00203-0, 1996.

Resler, J., Krč, P., Belda, M., Juruš, P., Benešová, N., Lopata, J., Vlček, O., Damašková, D., Eben, K., Derbek, P., et al.: PALM-USM v1. 0: A new urban surface model integrated into the PALM large-eddy simulation model, Geoscientific Model Development, 10, 3635–3659, https://doi.org/10.5194/gmd-10-3635-2017, 2017.

Resler, J., Eben, K., Geletič, J., Krč, P., Roseckỳ, M., Sühring, M., Belda, M., Fuka, V., Halenka, T., Huszár, P., et al.: Validation of the PALM model system 6.0 in a real urban environment: A case study in Dejvice, Prague, the Czech Republic, Geoscientific Model Development, 14, 4797–4842, https://doi.org/https://doi.org/10.5194/gmd-14-4797-2021, 2021.

Resler, J., Bauerová, P., Belda, M., Bureš, M., Eben, K., Fuka, V., Geletič, J., Jareš, R., Karel, J., Keder, J., Krč, P., Patiño, W., Radović, J., Řezníček, H., Sühring, M., Šindelářová, A., and Vlček, O.: Challenges of high-fidelity air quality modeling in urban environments -

PALM sensitivity study during stable conditions, Geoscientific Model Development, pp. 1–35, https://doi.org/10.5194/egusphere-2024-1231, 2024.

Salamanca, F. and Martilli, A.: A new Building Energy Model coupled with an Urban Canopy Parameterization for urban climate simulations—part II. Validation with one dimension off-line simulations, Theoretical and Applied Climatology, 99, 345–356, https://doi.org/10.1007/s00704-009-0143-8, 2009.

Salim, M. H., Schubert, S., Resler, J., Krč, P., Maronga, B., Kanani-Sühring, F., Sühring, M., and Schneider, C.: Importance of radiative transfer processes in urban climate models: a study based on the PALM 6.0 model system, Geoscientific Model Development, 15, 145–171, https://doi.org/10.5194/gmd-15-145-2022, 2022.

Schoetter, R., Caliot, C., Chung, T.-Y., Hogan, R. J., and Masson, V.: Local Climate Zones for Urban Temperature Studies, Boundary-Layer Meteorology, 189, 103–138, https://doi.org/10.1007/s10546-023-00827-9, 2023.

Skamarock, W. C., Klemp, J. B., Dudhia, J., Gill, D. O., Barker, D. M., Duda, M. G., Huang, X.-Y., Wang, W., Powers, J. G., et al.: A Description of the Advanced Research WRF Version 4, NCAR technical note, https://doi.org/https://doi.org/10.5065/1dfh-6p97, 2019.

Stewart, I. D. and Oke, T. R.: Local Climate Zones for Urban Temperature Studies, Bulletin of the American Meteorological Society, 93, 1879–1900, https://doi.org/10.1175/BAMS-D-11-00019.1, 2012.

Suter, I., Grylls, T., Sützl, B. S., Owens, S. O., Wilson, C. E., and van Reeuwijk, M.: uDALES 1.0: a large-eddy simulation model for urban environments, Geoscientific Model Development, 15, 5309–5335, https://doi.org/10.5194/gmd-15-5309-2022, 2022.

Tewari, M., Chen, F., Wang, W., Dudhia, J., LeMone, M. A., Mitchell, K., Ek, M., Gayno, G., Wegiel, J., and Cuenca, R. H.: Implementation and verification of the unified NOAH land surface model in the WRF model, in: 20th conference on weather analysis and forecasting/16th conference on numerical weather prediction, pp. 11–15, https://www2.mmm.ucar.edu/wrf/users/physics/phys_refs/LAND_SURFACE/noah.pdf, 2004.

Thompson, G., Field, P. R., Rasmussen, R. M., and Hall, W. D.: Explicit Forecasts of Winter Precipitation Using an Improved Bulk Microphysics Scheme. Part II: Implementation of a New Snow Parameterization, Monthly Weather Review, 136, 5095 – 5115, https://doi.org/10.1175/2008MWR2387.1, 2008.

Toparlar, Y., Blocken, B., Maiheu, B., and van Heijst, G. J. F.: A review on the CFD analysis of urban microclimate, Renewable and Sustainable Energy Reviews, 80, 1613–1640, https://doi.org/10.1016/j.rser.2017.05.248, 2017.

United Nations: World Population Prospects 2024: Summary of Results, UN DESA/POP/2024/TR/NO. 9, https://population.un.org/wpp/assets/Files/WPP2024_Summary-of-Results.pdf, [cited 8.10.2025], 2024.

Vieira Zezzo, L., Pereira Coltri, P., and Dubreuil, V.: Microscale models and urban heat island studies: a systematic review, Environmental monitoring and assessment, 195, 1284, https://doi.org/10.1007/s10661-023-11906-2, 2023.

Wallenberg, N., Lindberg, F., Holmer, B., and Thorsson, S.: The influence of anisotropic diffuse shortwave radiation on mean radiant temperature in outdoor urban environments, Urban Climate, 31, 100 589, https://doi.org/10.1016/j.uclim.2020.100589, 2020.

Wang, Y. and Akbari, H.: The effects of street tree planting on Urban Heat Island mitigation in Montreal, Sustainable Cities and Society, 27, 122–128, https://doi.org/10.1016/j.scs.2016.04.013, 2016.

Willmott, C. J.: ON THE VALIDATION OF MODELS, Physical Geography, 2, 184–194, https://doi.org/10.1080/02723646.1981.10642213, 1981.

World Meteorological Organization: Guide to Instruments and Methods of Observation, Volume III – Observing Systems, WMO-No. 8, https://doi.org/10.59327/WMO/CIMO/3, [cited 8.10.2025], 2024.

Yang, S., Wang, L., Stathopoulos, T., and Marey, A. M.: Urban microclimate and its impact on built environment – A review, Building and Environment, 238, 110 334, https://doi.org/10.1016/j.buildenv.2023.110334, 2023.